Comprehensive Fluid Saturation Study for the Fula North Field Muglad Basin, Sudan

by

Abdalmajid I. H. Altayeb

Thesis presented in partial fulfilment of the requirements for the degree of ***Master of Science*** *at the University of The Western Cape*

Departement of Earth Sciences,
University of the Western Cape,
Bellville, South Africa.

Supervisor: Dr. Mimonitu Opuwari

September 2016

Abstract

Comprehensive Fluid Saturation Study for the Fula North Field Muglad Basin, Sudan

A.I. H Altayeb

Departement of Earth Sciences,
University of the Western Cape,
Bellville, South Africa.

Thesis: MSc

September 2016

This study has been conducted to accurately determine fluid saturation within Fula sub-basin reservoirs which is located at the Southern part of the Republic of Sudan.
The area is regarded as Shaly Sand Reservoirs. Four deferent shaly sand lithofacies (A, B, C, D) have been identified. Using method based on the Artificial Neural Networks (ANN), the core surrounding facies, within Fula reservoirs were identified. An average shale volume of 0.126 within the studied reservoirs was determined using gamma ray and resistivity logs. While average porosity of 26.7% within the reservoirs was determined using density log and the average core grain density. An average water resistivity of 0.8 Ohm-m was estimated using Pickett plot method. While formation temperature was estimated using the gradient that constrained between surface and bottom hole temperature. Water saturation was determined using Archie model and four shaly sand empirical models, the calculation was constrained within each facies zone to specify a model for each facies, and another approach was used to obtain the water saturation based on Artificial Neural Networks. The net pay was identified for each reservoir by applying cut-offs on permeability 5 mD, porosity 16%, shale volume 0.33, and water saturation 0.65. The gross thickness of the reservoirs ranges from 7.62m to 19.85m and net pay intervals from 4.877m to 19.202m.

The study succeeded in establishing water saturation model for the Fula sub-basin based on neural networking which was very consistent with the core data, and hence has been used for net pay determination.

UNIVERSITY of the
WESTERN CAPE

Declaration

I declare that Comprehensive Fluid Saturation Study for the Fula North Field Muglad Basin, Sudan is my own work, that it has not been submitted before for any degree or examination in any other University, and that all the sources I have used or quoted have been indicated and acknowledged by means of complete references.

Abdalmajid. I. H. Altayeb

September 2016

Acknowledgements

Firstly, I would like to express my sincere gratitude to my supervisor , Dr. Mimonitu Opuwari,for the continuous support of my project, for his patience, motivation, and immense knowledge. His guidance helped me in all the time of research and writing of this thesis.

Also I would like to thanks the Earth Science Department of University of the Western Cape, for providing good atmosphere which help me in completion of this project.

I am loosing the words to thanks my colleague Traig Hammad for his precious support and valuable discussions.

special thanks to Sudanese ministry of petroleum for providing all data needed for this project

Last but not the least, I would like to thank my family: my parents and to my brothers and sister for supporting me spiritually throughout writing this thesis and my my life in general.

Contents

UNIVERSITY of the
WESTERN CAPE

List of Figures

UNIVERSITY of the
WESTERN CAPE

List of Tables

Chapter 1

Introduction

Reservoir characterization is process of quantitatively assigning reservoir parameters, as well as identifying the spatial distribution of these parameters. This process is achieved via the interpretation of continuous vertical recordings of physical and chemical properties of the subsurface formation taken by well logs. The process also involves integration of different datasets from multiple disciplines for better reservoir description(Gunter et al., 1997). Datasets include core measurements, seismic measurements, with well testing used to improve the well logs petrophysical model. Limited core data presents an important means to calibrate a petrophysical model due to its accuracy (Al-Saddique et al., 2000). The aforementioned parameters include porosity which gives an idea of the ability of the formation to store fluid. Permeability, extends to which the pores are interconnected and allows fluids to flow. And water saturation which has great influence in reservoir management. Given that all fluid saturations (water and hydrocarbons) should add up to unity, an accurate calculation for water saturation is a key factor for estimating hydrocarbon storage within a reservoir to better assess the reservoir's economic viability.

1.1 Research aims and Objectives

The main objective of this study is to accurately determine water saturation for the Fula north field, in order to identify the gas/oil or oil/water contacts by changes of residual saturation with depth. This can be achieved by calculation of water saturation through different methods using all available data. Core data will be used to validate the outcomes of these methods in order to choose the most consistent approach for the net pay calculation.

The process for achieving the aforementioned requires:

- Performing data quality control through the environmental corrections for well logs and overburden correction for the core data.

- To investigate the reservoir sedimentological characteristics of the basin strata and predict the lithofacies.
- Estimate petrophysical properties and volume of shale from the well logs data.
- Calculate water saturation using different methods including the Archie model, shaly sand models, and neural networks.
- To calculate the net pay of the studied reservoirs using the most consistent approach of water saturation.

1.2 Location of the Study Area

The Muglad Basin is located in southern part of the Republic of Sudan, and expands to the northern part of the Republic of South Sudan . The Fula sub-basin is fault-bounded half- graben located in the NNE part of Muglad Basin as shown in figure 1.1. Four wells were selected for this study: FN-92, FN-12, FN-10, and FN-94. The distribution of the studied wells across the Fula sub-basin is shown in figure 1.2.

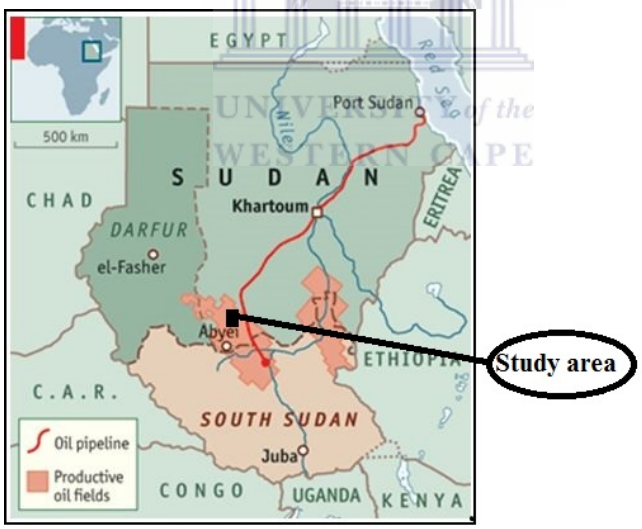

Figure 1.1: Location of the study area (Hussien, 2012)

1.3 Data Set

Three data sets were collected for this study:
- Conventional core analysis data from the well FN-12.
- Special core analysis data from the well FN-12.

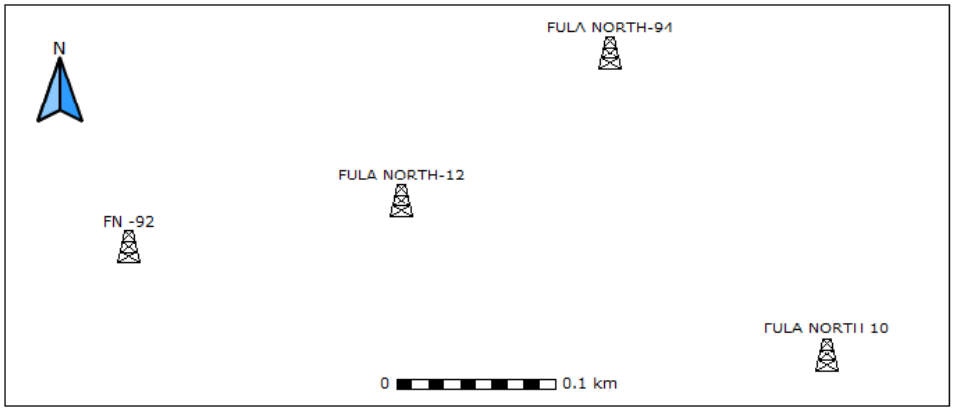

Figure 1.2: Distribution of the studied wells across the Fula sub-basin

- Wire line logs of all studied wells.

All the data used in this project was provided by the ministry of petroleum (Sudan).

1.4 Thesis structure

This thesis is the written report of the research carried out to evaluate the fluid saturation of the Fula North field, Muglad Basin. In chapter one a general introduction to the study is given. The structure and sequences stratigraphy of the Muglad Basin are reviewed in the second chapter. A review of the Archie and shaly sand interpretation models as well as the effect of clay on logs response are given in chapter three. The fourth chapter presents the methodology of the study, with the corrections applied to the core and wireline data. Reservoir zones and Facies distribution within the aforementioned zones and detailed petrophysical model is presented in chapter five. Chapter six presents the determinations of the cut-off values and net pay of the studied reservoirs. With chapter seven covering remarks and conclusions drawn from the study.

Chapter 2

Geological setting of the study area

In this chapter, a description of the Muglad Basin is presented. This description introduces the structural development in order to study the stratigraphy in details, from which the sedimentation history might be determined. The Muglad Basin covers an area of approximately $150,000\text{km}^2$, 750 km in length and 200 km in width. It is one of the largest intra-continental rift system formed in world due to central Africa shear zone (CASZ). The Basin is oriented NW-SE which expanded from the southern part of the Republic of Sudan to the northern part of the Republic of South Sudan . The location of Muglad Basin and Fula north field is shown in figure 2.1

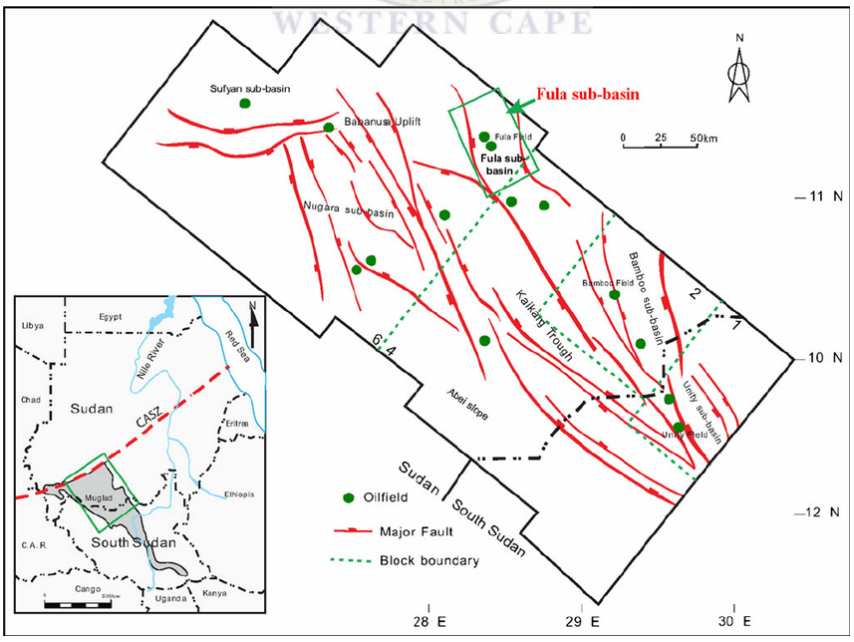

Figure 2.1: The location map of the Muglad Basin, north-south Sudan (Lirong et al., 2013)

2.1 Tectonic and structure

The African rift system, which was initiated in the Late Jurassic to Early Cretaceous period, lead to the separation of the African and South American cratons (Schull, 1988) resulting in major shear reactivation along the Central African Shear Zone.Fairhead (1988) refers the central African rift system to the differential opening of south, equatorial, and central Atlantic Ocean. However, this led to the Central and Southern Sudan Interior Rift Basins development which formed parallel and subparallel half grabens of predominantly NW-SE orientation. The development of those rift basins is consider to be as result of processes operating within the central areas of Africa as well as along the eastern and western continental margins of Africa. Further, triple junction was initiated during the late Jurassic period along the Kenya coastline, separating Malagasy island from the African continent. The failed arm of that triple junction extended from the Lamu Embayment through Anza Trough in northern Kenya into southern Sudan. This relation of rift systems within the African plate can be seen from the extensional stress that have been created due to the differential opening of the Atlantic and Indian Oceans (Fairhead, 1988). These series of grabens include the Blue Nile Rift, White Nile Rift, Melut Rift, Muglad Rift and Baggara Basin. The rifting continued to Middle Miocene and three periods of rifting (140-95 Ma, 95-65 Ma, 65-30 Ma) was recognized (Schull, 1988). Those periods led to the accumulation of more than 5 km of sediments in the Muglad Basin. Using geophysical data, well information and regional geology Schull (1988) divided the structural development of the Sudan into pre-rifting, rifting, and sag phases.

2.1.1 Pre-rifting Phase

The pre-rifting phase was the period after the end of the Pan-African orogeny (550 ± 100Ma) when the region became a consolidated platform. There was a site of sediments and alkaline magmatism probably due to subsiding of the mantle plume during Paleozoic to the Late Jurassic (Vail, 1985; Schandelmeier et al., 1993). The general lack of lithic fragments in the oldest rift sediments suggests that no significant accumulation of sedimentary section existed in the area prior to rifting (Schull, 1988).

2.1.2 Rifting Phases

According to the crustal extension there was three periods of rifting (Browne and Fairhead, 1983). The early rifting phase cannot be accurately dated, but it is thought to have begun in the Late Jurassic to Early cretaceous period (130 - 160 Ma) and lasted to almost the end of Albian. Subsidence was achieved by normal faulting parallel and subparallel to the basinal axis. Volcanism has not been recognized within this rifting phase inside Sudan.

However, the end of this phase is stratigraphically marked by a basin wide deposition of the sandstone of the Bentiu Formation (Schull, 1988).

The changes in the opening of the southern Atlantic Ocean during the late Cretaceous period resulted in shear movement along the west and central African rift system, this has led to dextral reactivation along the central African fault zone, which led to the second rifting phase (Fairhead, 1988). The second rifting phase occurred at the time between the Turonian - Late Senonian age. Stratigraphically, this phase is characterized by the widespread deposition of lacustrine and floodplain claystones and siltstones, which sharply ended the deposition of the Bentiu Formation , as well as minor volcanism activity (Schull, 1988). Stratigraphically, the end of the phase is marked by the deposition of an increasingly sand-rich sequence that concluded with thick Paleocene sandstone; the Amal Formation. The final phase was simultaneous to the opening of the Red Sea during the Late Eocene - Oligocene period,a thick sequence of lacustrine and floodplain claystones and siltstone has marked this phase (Lowell and Genik, 1972). The occurrence of a late Eocene basalt flows in the southern Melut basin close to Ethiopia is considered to be the evidence of volcanism during that phase. However, age dating of the widely scattered volcanic outcrops indicates volcanism in the Sudan at the time (Vail, 1978). After this period of rifting throughout the Late Oligocene - Miocene, deposition became that of a more sand-rich sediment.

2.1.3 Sag phase

In the middle Miocene period, the basinal areas entered an intracratonic sag phase of very gentle subsidence accompanied by little or no faulting. In the Muglad and Melut Basins the Eocene - Oligocene sedimentation continued across the Oligocene/Miocene boundary with the deposition of basin wide fluvial and floodplain sediments of the upper members of the Kordofan Group. Limited outcrops of volcanic rock in the area southeast of Muglad dated at $5.6Ma \pm 0.6$ m.y. and $2.7Ma \pm 0.8$ m.y. indicate that minor volcanism occurred locally. However, during that time, extensive volcanism occurred in some adjoining areas to the north (e.g., Marra Mountain and Meidob Hills), as well as to the south and southeast of the Melut Basin in Kenya and Ethiopia.

Structurally the area is dominated by dip-slip normal faults. The three rifting phases resulted in a long complex history of horst and graben development and the formation of a highly complicated fault system. The predominant fault orientation is parallel or subparallel to the strike of the primary grabens and basin margins. These longitudinal faults mainly strike $N40 - 50W$ throughout the Muglad, Melut, and Blue Nile Basins. Older NNW trends also exist in the central and southern Muglad Basin.The faults within

these basins are commonly oblique to the primary trends. Few transverse faults occur relatively. Faults also show variety in displacement, geometry, and growth history (Schull, 1988). Seismic data indicates that the prospective structures formed by this complex extensional history can be categorized as:

- Rotated block faults which are formed by simple block rotation along normal fault planes. The entrapment in such structure depends upon the seal across the fault.
- Drape folds which are formed in the sediments overlying the upthrown side of deeper normal faults. This type has been found in areas where faults formed during the early rifting phase were not reactivated.
- Downthrown rollover anticlines which are formed by rotation into listric faults. These listric faults are associated with antithetic faults subparallel to the primary fault trend.

2.2 Stratigraphy of Muglad Basin

According to Mohamed et al. (2001), every rifting phase was followed by subsidence and sedimentation . The consecutive rifting in the Muglad Basin has resulted in three cycles of deposition. The Sharef, Abu Gabra, and Bentiu Formations represent the first cycle,the second cycle by the Cretaceous of Darfur Group and the third cycle by Kordofan Group (Mohamed and Mohammed, 2008; Giedt, 1990). The age of the cycles are in order; Late Jurassic to Cenomanian, Turonian to Paleocene,and Early Tertiary.

2.2.1 Basement complex

The majority of the basement adjacent to the Muglad Basin is Precambrian and Cambrian metamorphic rocks with limited outcrops of intrusive igneous rocks, the main composition consist of granitic Gneiss, granodioritic gneiss, mica and graphitic schists and metavolcanic rock. According to Schull (1988) the basement that has been penetrated within the Muglad Basin was granitic gneiss and granodioritic gneiss dated 540Ma $\pm$ 40m.y.

2.2.2 First cycle strata

The first cycle happened after the first rifting phase during Early Cretaceous to Albian Time, which consists of the previously mentioned The Sharef, Abu Gabra, and Bentiu Formations. During the early rifting phases Neocomian-Barremian claystones, siltstones and fine grained sandstones of the Sharaf Formation were deposited in the fluvial-floodplain and Lacustrine environments. The period from Aptian-early Albian represents the period of greatest lacustrine development . Several thousand feet of organic-rich lacustrine claystones and shales of the Abu Gabra Formation were deposited along with interbedded

fine-grained sands and silts. The nature of this deposit was likely the result of a humid climate and the lack of external drainage, indicating that the basins were tectonically silled. The Abu Gabra Formation is estimated to be up to 6,000 ft. (1,829 m) thick. In the northwestern Muglad block, these sands were deposited in a lacustrine-deltaic environment. The lacustrine claystones and shales of this unit are the primary source rock of the interior basin (Sayed, 2003). The cycle termination is indicated by the deposition of bentiu formation during the late Albian-Cenomanian, and widespread of alluvial and fluvial-floodplain environments, possibly due to a change from internal to external drainage. The regional base level, which was created by the earlier rifting and subsidence, no longer existed. Those thick sandstone sequences were deposited in braided and meandering streams. This unit, which is up to 5,000 ft. (1,524 m) thick, typically shows good reservoir quality. Sandstones of the Bentiu Formation are the primary reservoirs of the basin (Schull, 1988).

2.2.3 Second cycle strata

The second cycle occurred during the Turonian-Late Senonian as a consequence of the second rifting phase. It starts with the deposition of the Darfur Group, which represents a cycle of fine to coarse-grained deposition and includes four Formations (Lirong et al., 2013). The lower portion of the group consists of the Aradeiba and Zarqa Formations, characterized by the predominance of claystone, shale, and siltstone. The excellent regional correlation of this unit verifies the strong tectonic influence sedimentation. Floodplain and lacustrine deposits were widespread. The low organic carbon content indicates deposition in shallow and well oxygenated waters. These units may represent a time when the basins were partially silled, the Aradeiba and Zarga Formations acting as an important seal. Interbedded with the floodplain and lacustrine claystones, shales, and siltstones are several fluvial/deltaic channel sands generally 10-70 ft (3-21 m)thick. The Cretaceous period ended with the deposition of increasingly coarser grained sediments, reflected in the higher sand percentage of the Ghazal and Baraka Formations. These units were deposited in sand-rich fluvial and alluvial fan environments, which prograded from the basin margins. The Darfur Group is up to 6,000 ft (1,829 m) thick. This second cycle ended with the deposition of Amal Formation which consists of thick massive sandstones, dominantly composed of coarse to medium-grained quartz arenites. This formation represents high energy deposition in a regionally extensive alluvial-plain environment with coalescing braided streams and alluvial fans. These sandstones are potentially excellent reservoirs. (Schull, 1988).

2.2.4 Third cycle strata

The third rifting phase was created by the reactivation of extensional tectonism during the Late Eocene- Oligocene period. The syn-rift sediments of this cycle consists of the Nayil and Tendi Formations, which represent the middle section of the Kordofan Group . These formations are dominated by claystones deposited in fluvial/ floodplain and lacustrine environments. The third cycle ended the deposition of the Adok and Zeraf Formations, during Late Oligocene to Middle Miocene/ Recent period. Sandstones and sands dominate the Adok and Zeraf Formations, with only minor clay interbeds appearing. Deposition happened mainly in braided stream environments. However, the deposits of this interval appear to only have a minor oil source potential; they offer excellent potential as a seal overlying the massive sandstones of the Amal Formation (Sayed, 2003). A generalized stratigraphic column of Muglad Basin is shown in figure 2.2.

2.3 Fula sub-basin

The Fula sub-basin is fault-bounded half-graben located in the NNE part of Muglad Basin covering an area of $3560 km^2$ as shown in figure 2.3. It trends northwest-southeast in the same general trend of the Muglad Basin, the sub-basin is bounded by two sets of faulting. The first, is striking NW which dominates the evolution and sedimentary of the Fula Structural Play. The second set striking EW, controls the evolution of the trap (Hussien, 2012). The interpretation of seismic data and drilling results indicates that the sedimentary column in the Fula sub-basin is up to 8400 m thick. As with the Muglad Basin, the Fula sub-basin has been subjected to three rifting phases followed by the sag phase. This resulted in a succession of four sequences separated by unconformities, and their related conformities as follows:

- Lower Cretaceous
- Upper Cretaceous
- Paleogene
- Neogene-Quaternary

The greatest extension recorded was during the early Ceretaceous rifting phase, which is marked by a deposition of medium- to coarse-grained fluvial sandstone interbedded with thin claystones and thick organic rich laminated shales of the Abu Gabra formation; representing the main source rock throughout the Muglad Basin (Lirong et al., 2013). However, the extension became weaker during the late Cretaceous rifting episode, which is marked by deposition of fluvial to shallow lacustrine sandstones of Bentiu Formation. These sandstones, up to 800m thick, are the most important reservoir rock in the sub-basin (Lirong et al., 2013).The Bentiu Formation is bounded above by the Darfur Group, also up

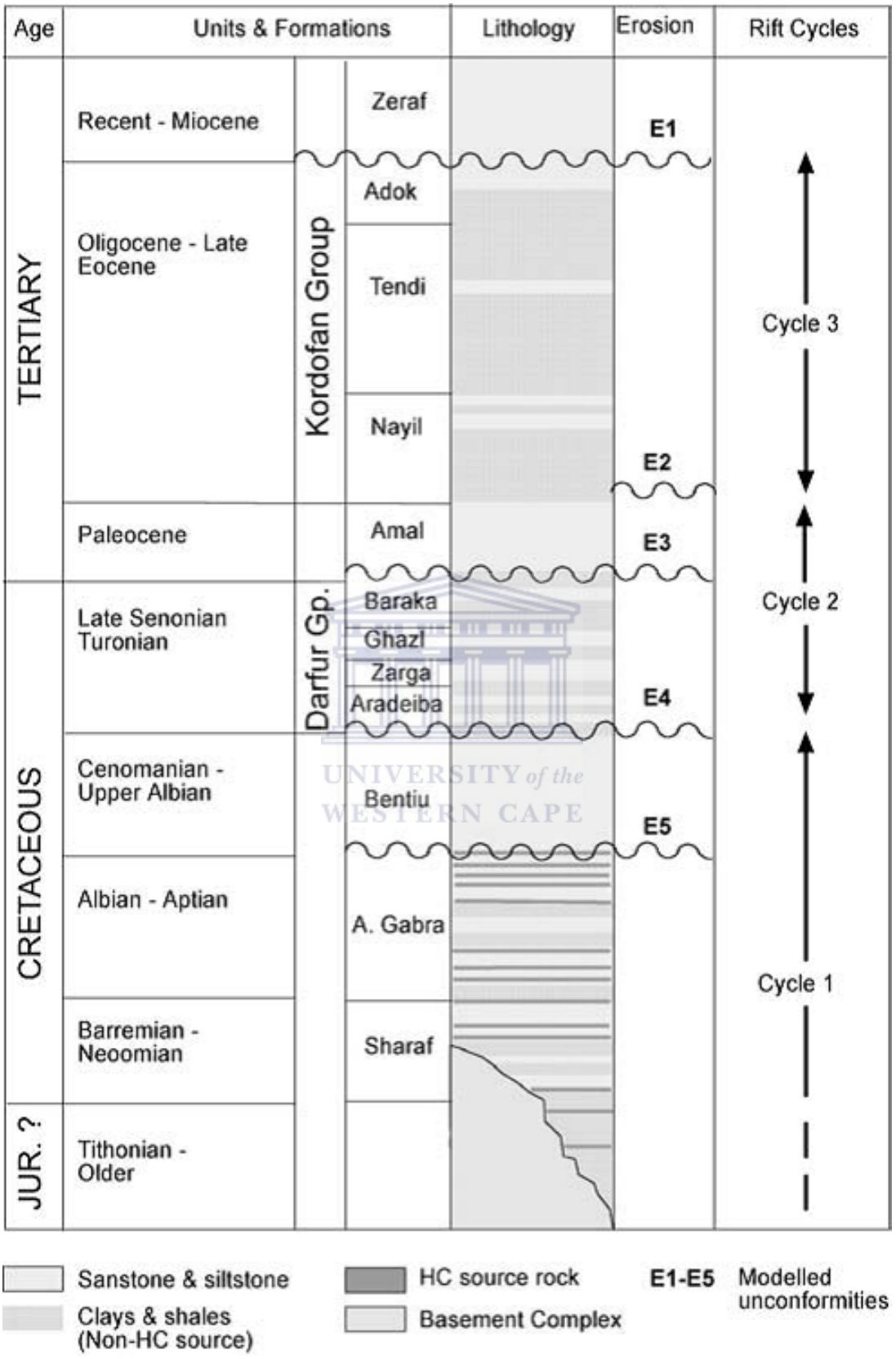

Figure 2.2: Generalized stratigraphic column of Muglad Basin (Makeen et al., 2015)

to 800 m thick, which consists of fluvial floodplain and shallow-lacustrine sediments. Grey and green claystones occur in the Aradeiba and Zarqa Formations, and sandstones in the Ghazal and Baraka Formations. During the Paleogene period rifting became stronger and was simultaneous to the opening of the Red Sea. However, as represented by the Kordofan Group, this is not well developed in the Fula sub-basin. The Group is about 500 m thick. Claystones are dominant in the lower interval and overlying is mainly sandstones.

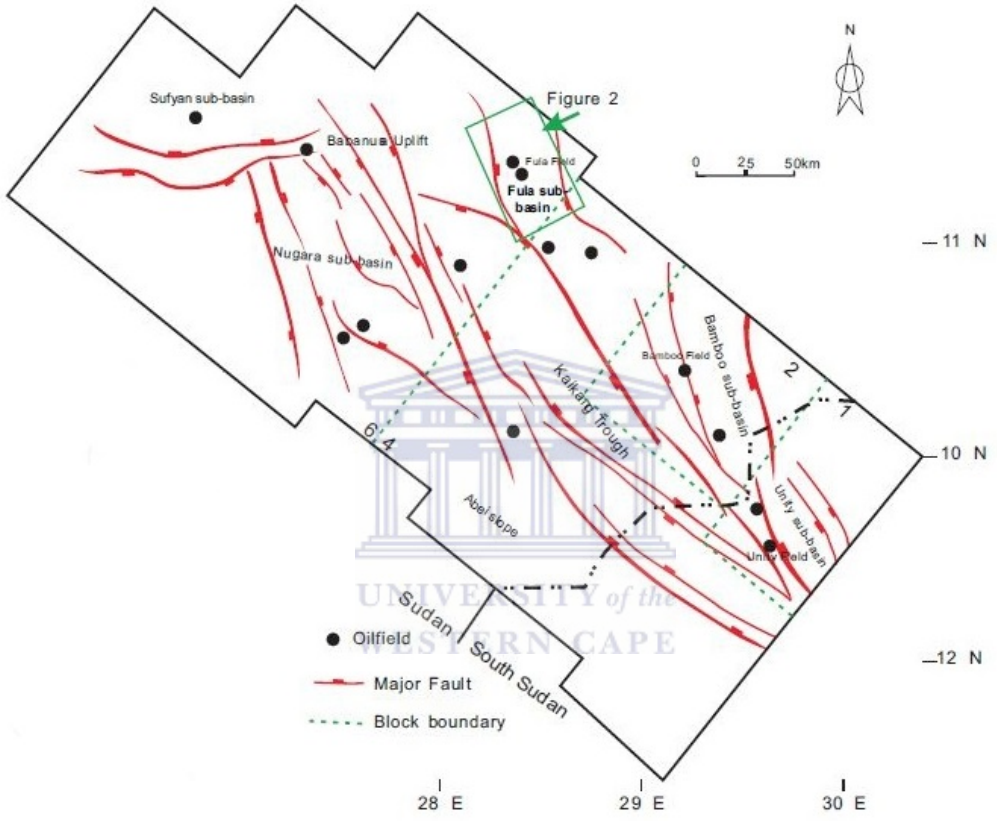

Figure 2.3: Structural unit in the Muglad basin including Fula sub-basin and oil fields discovered so far (Lirong et al., 2013)

Chapter 3

Review on saturation models and shale effect on log response

In this chapter, a review of water saturation models within shaly sand reservoirs and their advantages and disadvantages is discussed. The clay minerals and their influence on influence reservoir characteristics and logs response is also discussed.

3.1 The general properties of clay minerals

Clays refer to particle diameter size less than 0.0625 mm. Clay minerals consist of mainly hydrated alumino silicates with small amounts of magnesium, iron, potassium, and other elements (Kurniawan, 2005). Clays are often found in sandstones, siltstones, and conglomerates. These sedimentary rocks are usually deposited in high-energy environment. A mixture of clays minerals and other fine-grained particles deposited in a very low- energy environment is referred to as shales. Clays are usually sheet-like particles made by stacking of lattices of aluminum octahedral or silica tetrahedral, these sheets are having very large surface compared to their volume (Waxman and Smits, 1968). A negative electrical charge will be created inside the clay sheet when a magnesium ion (MG^{+2}) substitutes an aluminum ion (AL^{+3}) in the octahedral lattice. In order to maintain the electrical neutrality of the clay particle in saline solution, clays will loosely hold some additional cations (NA^{+}, K^{+}) in a diffuse layer on their surface. The number of the compensating ions or counterions is represented by the Cation Exchange Capacity (CEC). CEC is expressed in milliequivalents per gram of dry clay (1meq = 6x1020atoms). It may also be expressed in term of milliequivalents per unit volume of pore fluid; Qv. The higher the number of cations, the higher the CEC in the formation(Waxman and Smits, 1968).

3.2 Distribution and effects of Clays within sedimentary rocks

The presence of clay content which results in shale layers influences reservoir rock according to its amount, physical properties, and the way the shale is distributed in the formation. According to Ellis and Singer (2008) there are several influences caused by the shale in the reservoir:

1) Decrease in effective porosity.

2) Result in fine grains of clay minerals filling the pore throat which decrease the permeability.

3) Influences logging tools response.

4) Increasing the apparent Neutron log porosity in case of the presence of hydrogen associated with the clay.

5) Presence of clay minerals affect the conductivity of the formation and lead to inaccurate water saturation results.

Shale is mainly distributed in three forms according to (Schlumberger, 1989) as shown in figure 3.1:

-Laminar shale; the occurrence of shale in the form of laminae between which are layers of clean sand, this type does not affect the porosity or permeability of sand, but it does decrease the effective porosity as it increase in volume.

-Structural shale; the occurrence of shale as grains or nodules within the formation matrix, it is usually considered to have the same properties as laminar shale.

-When the shale is dispersed throughout the sand, partially filling the pore channels which directly decrease formation permeability; it is in the form of dispersed shale.

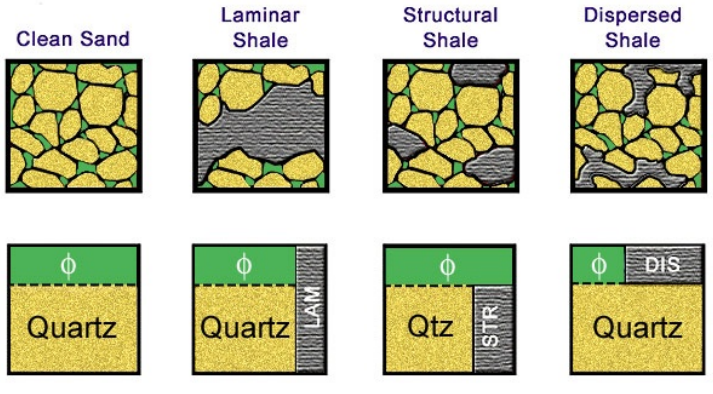

Figure 3.1: Shale distribution patterns ((Schlumberger, 1989)).

3.3 The effect of clays on log response

The presence of shale in subsurface formation affects every logging tool to some degree depending on the type and amount of clay minerals of shale. Figure 3.2 shows the typical log response of shale presence in formation, which result in the log reading gradually displaced towards the shale line as shale increases (Bassiouni, 1994) . Shale also causes the calculated values of porosity to be too high due to:
the high interval transit time of shale, causing it to be high when calculated by sonic log. shale containing a high concentration of hydrogen ions, predicting high porosity if neutron log is used in the calculation. While it could be high or low using a density tool as it depends on shale and formation matrix density; with a low calculated porosity if the shale density is greater than matrix density and vice versa (Kamel. and Mabrouk., 2003).

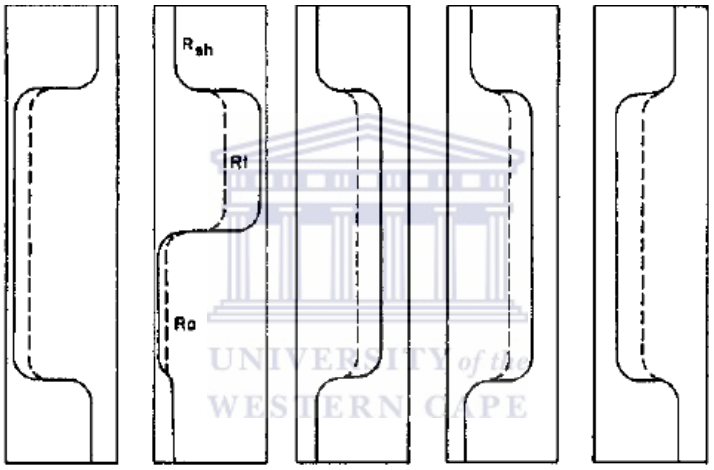

Figure 3.2: Shale effect on log response (Bassiouni, 1994).

Shale also affects a resistivity tool reading, because it has the ability to absorb pore water to their surface. This bound water contributes to the additional electrical conductivity or lower resistivity of shaly sand formation. Furthermore, the clay surfaces will seek neutrality, therefore it exchange cations (CEC) between the clays bound water and free water, which also causes an increase in the surface electrical conductivity. Thus, the greater the CEC of clays in shaly sand, the more the resistivity will be lowered (Bush and Jenkins, 1977). On the other hand shales are classified into two groups, effective shale which has significant CEC while passive shale has essentially zero CEC (Hamada, 1996). However, effective shales show different surface areas according to their crystal structure, thus showing different CEC values. Demonstrating the non uniformity of the electrical effect of clay, as shown in figure(3.3) where the formation resistivity factor F or Cw/Co is plotted against the conductivity of rock fully saturated by water Cw. The figure indicates the effect of clay is not uniform; especially, at a lower salinity where the relationship has

deviated significantly from that of a clean sand line. This also means at lower salinity the formation resistivity is more reduced. Without reliable evaluation methods, the chance of over-looking hydrocarbon zones is greatly increased.

3.4 Shaly sand reservoir characteristics

Many authors have published several models to overcome the presence of clay minerals in the reservoir, but most are empirical fits to local data and lack universal application (Bassiouni, 1994) These models could be divided into two categories: volume of shale models, and double layer models.
Prior to 1950 petrophysicists had been considering a reservoir as clean layer (shale free) in subsurface formation. This means that water is the only conductive component within the reservoir. This is the assumption from which Archie derived his equation (Archie, 1942):

$$S_w^n = \frac{FR_w}{R_t} \tag{3.1}$$

where:
R_w = resistivity of formation water, ohm/m.
R_t = resistivity of formation rock, ohm/m.
S_w = formation water saturation, fraction.
n = saturation exponent.
F = formation resistivity factor which is defined as a ratio of formation resistivity (R_o) to formation water resistivity (R_w).

$$F = \frac{R_0}{R_w} \tag{3.2}$$

For the fixed values of water resistivity (R_w) the value of F will vary according to the rock porosity, the lower the porosity, the higher the formation resistivity (R_o) will be and therefore F values (Ellis and Singer, 2008). Hence the relationship between F and porosity is controlled by the grain cementation, so this relationship can be expressed as:

$$F = \frac{1}{\Phi^m} \tag{3.3}$$

where:
Φ = formation porosity.
M = cementation exponent.

The Archie equation provided quantitative petrophysical evaluation basis. Furthermore, it gives reliable results especially when dealing with clean formation, but the presence of shale in the reservoir will lead to misleading results when evaluating a reservoir using Archie equation due to excess conductivity of shale can led to overestimation of water saturation. The way that shale affects the electrical conductivity of the reservoir rock is illustrated in Figure 3.3. The figure shows the conductivity of water saturated sandstone (C_o) as function of water conductivity (C_w).
The first case where the formation is clean, represents the application of Archie's equation, so it is straight line with gradient (-m). The other case where the formation with same effective porosity, but some of the matrix is replaced by shale, the line lies upward the clean sand line which means (C_o) has increased. This increase of conductivity is due to shale and known as the excess conductivity (C_{excess}). Also the terms linear and nonlinear zone shown in the figure are referring to the fact that the absolute quantity of excess conductivity is not constant for a given sample with variation in water conductivity, actually it increases as C_w increases (nonlinear zone) until it become constant even if C_w is still increasing (linear zone) (Kurniawan, 2005).

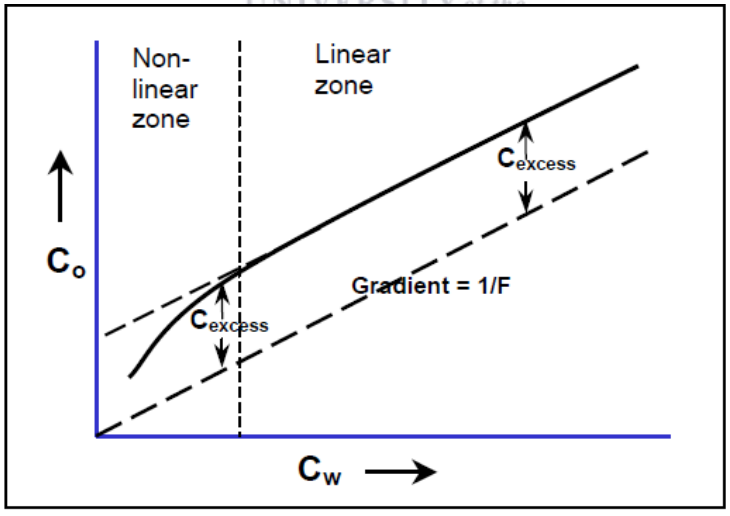

Figure 3.3: Shale effect on electrical conductivity (Kurniawan, 2005)

.

As the Archie equation is not valid for all formations, petrophysicists seek equations that account for the shale excess conductivity by adjusting the Archie equation to include the excess conductivity within a composite shale-conductivity term X. It was proposed that

the following formula is valid for all granular reservoirs that are fully water saturated (Worthington, 1985).

$$C_o = \frac{C_w}{F} + X \tag{3.4}$$

This equation could be reduced to the Archie equation if C_w is very large so X has little influence on C_o , since X is almost zero for clean formations where Archie equation applies well. Conversely, the ratio C_w/C_o is effectively equal to the intrinsic formation factor F only if X is sufficiently small and/or C_w is sufficiently large. Thus, although the absolute value of X can be seen as a shale contribution to formation conductivity, the manifestation of shale effects from an electrical standpoint is also controlled by the value of X relative to the term C_w/F.

Many models have been published to address the excess conductivity problem, depending upon how they define X in equation 3.4 these models could be divided into two main groups:

3.4.1 Volume of shale models

The main approach of volume of shale models group is to solve the interpretation problem in calculating porosity and saturation values free from the shale effect. This shale effect depends on the number of shale content in the formation, thus the determination of volume of shale V_{sh} is a critical step. Volume of shale Vsh is defined as the volume of wetted shale per unit volume of reservoir rock. The term wetted shale means that the bound water (water that covers the surface of the shale grains) is considered when calculating total porosity. These models are applicable to logging data without the need to a core sample calibration of the shale related parameter. None of the models can accommodate both linear and nonlinear zone as shown in figure 3.3 and a correction made in one zone will lead to the mismatch of another zone, thus leading to misinterpretation if not carefully applied due to its limitation. (Worthington, 1985). Another disadvantage of volume of shale models is that they only deal with shale volume, regardless of its distribution or mineral composition. Since clay mineral variation can result in different shale effects for the same volume of shale. Earlier models were based on the assumption that the conductivity of an aggregate of conductive particles saturated with conducting fluid can be represented by resistors in parall (Lee and Collett, 2006).

Based on the aforementioned definition of shale volume, and its relation with the total porosity Hossin (1960) develop a model assuming that in shaly sand formations wetted shale V_{sh} occupies pore space gradually so it correspond to Archie's porosity. Further,

in the Archie equation the conductivity of the material occupying pore space is C_w is replaced by C_{sh} in this model. Therefore in this model the conductivity equation is derived as follows Assuming that cementation factor equal to 2, the Archie equation can be written in the following form:

$$C_o = \phi^2 C_w \tag{3.5}$$

Then replace ϕ and C_w by V_{sh} and C_{sh} respectively to get shale term (X)

$$X = V_{sh}^2 C_{sh} \tag{3.6}$$

Hence the conductivity equation for Hossin's model expressed as

$$C_o = \frac{C_w}{F} + V_{sh}^2 C_{sh} \tag{3.7}$$

Simandoux (1963) used the concept of the aggregate conductivity of conductive particles saturated with conducting fluid which can be represented by resistors in parallel, thereby proposing a shaly sand model that shows the conductivity of the formation to be the sum of the conductivity through the water and the conductivity through the clay minerals. He examined a homogeneous mixture of sand and montmorillonite and represents the shale term (X) as

$$X = V_{sh} C_{sh} \tag{3.8}$$

With the conductivity equation of Simandoux model expressed as

$$C_o = \frac{C_w}{F} + V_{sh} C_{sh} \tag{3.9}$$

The linear form of the Hossin and Simandoux equations means that they can only accommodate the linear zone on figure 3.3 as none of the volume of shale models accommodates both zones, yet. The montmorillonite used in the Simandoux experiment was not fully wetted and that is why the model differs from the Hossin model in V_{sh} exponent.

Poupon and Leveaux (1971) noticed that the water saturation calculated in some Indonesian wells, where the reservoir rock is characterized by fresh formation water and high

degree of shaliness is overestimated, when one uses V_{sh} equal to the one in the Simandoux model. Thus they proposed a formula having an exponent that is itself a function of volume of shale. The model is known as the Indonesia model and expressed as

$$\sqrt{C_o} = \sqrt{\frac{C_w}{F}} + V_{sh}^{1-\frac{V_{sh}}{2}} \sqrt{C_{sh}} \tag{3.10}$$

So shale term (X)

$$X = V_{sh}^{1-\frac{V_{sh}}{2}} \sqrt{C_{sh}} \tag{3.11}$$

3.4.2 Double layer models

These models are based on unusual resistivity behavior when shale is present in sand formation. This behavior is described by (Winsauer and McCardell, 1953) as ionic double layer phenomenon. This was the basic concept used for those models.

Based on analysis of large number of water saturated shaly sand core samples Hill and Milburn (1956) reached a nonlinear relationship between formation resistivity and formation water resistivity. Their analysis also illustrates that the cation exchange capacity is a highly effective shale indicator. The method is limited though by its dependency on the core data.

The relation between formation water resistivity and formation resistivity is expressed as follows

$$\frac{R_o}{R_w} = F_a = F_{0.01}(100R_w)^{b\log(100R_w)} \tag{3.12}$$

where:
R_w = resistivity of formation water, ohm/m.
R_o = resistivity of formation rock, ohm/m.
F = formation resistivity factor.
$F_{0,01}$ = formation resistivity factor extrapolated to a hypothetical saturating solution of 0.01 ohms-m at 77^o F.
And b is CEC term expressed as:

$$b = \left(-0.135\frac{CEC}{PV}\right) - 0.0055 \tag{3.13}$$

where:
CEC = cation exchange capacity, meq/100 gm.
PV = pore volume, fraction.
Waxman and Smits (1968) extended on Hill and Milburn's work by using their data along with data where both oil and water are present in shaly sand. They developed a model that relates the conductivity of water-saturated shaly sand (C_o) to the shaliness factor (Q_v), conductivity of formation water (C_w), and porosity (Φ). The equation fit both Hill and Milburn's experimental data, and their data which was selected from shaly sand formation that consists of a wide range of cation exchange capacities. Mathematically it is expressed as:

$$C_o = \frac{1}{F^*}(BQ_v + C_w) \tag{3.14}$$

where:
F^* = shaly sand formation factor and given as:

$$F^* = \frac{1}{\phi^m} \tag{3.15}$$

Q_v = cation exchange capacity per unit volume.
B = equivalent conductance of sodium clay exchange cations (expressed as a function of C_w at 25_o C) it given as

$$B = \left[1 - 0.06e^{(-C_w/0.013)}\right] 0.046 \tag{3.16}$$

Juhasz (1981) proposed a more practical version of Waxman-Smits' model because the cation exchange capacity can be estimated in a continuous form from logs data on basis of clay mineralogical data that obtained from core data. The term Q_v in Waxman-Smits is replaced by Q_{vn} normalized Q_v. This Q_{vn} term is expressed as:

$$C_o = \frac{C_w}{F} S_w^n \left\{\frac{C_w}{F}\right\} \frac{Q_{vn} V_{sh} S_w}{\phi} \tag{3.17}$$

where:
Q_{vn} = Normalized cation exchange capacity per unit volume.
S_w = Water Saturation of the uninvaded zone.
ϕ = Rock porosity.
V_{clay} = Volume of clay.

ϕ_{clay} = Porosity of clay.
n = Saturation exponent.

Clavier et al. (1984), start from Waxman and Smits concept of formation conductivity as a combination of water conductivity and clay counterions. They relates each of the conductivities to particular type of water; clays bound water and free water. In other words sand formation behaves as clean formation, but with the water conductivity of a mixture from both components. The approach is called dual water; mathematically expressed as;

$$C_o = \frac{C_{we}}{F_o} \tag{3.18}$$

where:
C_{we} = equivalent conductivity of mixture water.
F_o = formation resistivity factor associated with total porosity.

$$C_{we} = (1 - V_Q Q_v)C_w + V_Q Q_v C_{cw} \tag{3.19}$$

where:
C_{we} = equivalent conductivity of mixture water.
V_Q= amount of clays associated with 1 unit (meq) of clays counterions.
Q_v = cations exchange capacity.
C_{cw} = conductivity of clays bound water.

Chapter 4

Data and methodology

This chapter describes the methods used to conduct the petrophysical model, the collected data types and the different editing methods used to correct the data. Three types of data were collected for the project: well logs from four wells, conventional and special core measurements from one well. To convert the well logs to accurate petrophysical parameters the logs must be edited, since the logging environment should be disturbed by the drilling process. It is therefore important to check the quality of the data, and perform the necessary editing before performing quantitative interpretation. All the data used in this project was collected from the ministry of petroleum (Sudan).

4.1 Methodology

The research involves a literature review of previous studies related to water saturation for oil and gas fields in order to understand the geology and details of hydrocarbon exploration within areas of the Southern Sudan region. To achieve the aims of this project:
-The high quality data set of the reservoir will be utilized. Including wireline data from all the studied wells and core data from the selected well. This data will carefully arranged, sorted, and prepared for easy access before being loaded into interpretation software.
-Lithofacies will be identified from the core reports; followed by combining the core data and wireline logs to predict electfofacies for the core surrounding intervals and other studied wells.
-Develop a petrophysical model dependent on wireline logs and core data to determine shale volume porosity, and water saturation. The core data will be used for correlation with logs calculation of the petrophysical parameters. All data to be loaded into Techlog software to perform the calculation.
-Two approaches will be used to calculate water saturation. The first approach based on shaly sand empirical models. The resultant water saturation curves will be validated

using core data. Comparison between the models will be done within each Lithofacies for more accurate results, since the models are based on local data.
-The second approach that will be used to determine water saturation in the studied reservoirs is artificial neural network. Followed by calibration with the core data for each approach outcomes to choose the most consistent approach for net pay calculation.
-Develop a written report

4.1.1 Wireline data

A conventional suite of wireline log was collected from four wells located in the Fula sub-basin. The logging was run by China national logging corporation (CNLC) in three wells, while the fourth one was run by Schlumberger Company. The logs used include:

- Caliper
- Gamma ray
- Deep laterolog
- Shallow laterolog
- Microspherecally focus log
- Density
- Sonic
- Neutron
- Photo electric cross section

Before processing the determination of the petrophysical parameters, the well logs quality were checked, and editing performed as required for environmental correction, and log normalization.

4.1.1.1 Environmental correction

After importing the wireline suites into the Techlog software, the data was checked before starting any further process, with environmental corrections done for the all well data. Because logging devices used during drilling should give true repeatable readings, that represent the undisturbed zone of subsurface formation, the drilling process will change the ideal conditions in which logs should measure the formation properties (Rider, 1996). The main factors that affect logging environment include the following;

Hole diameter A well's diameter depends on the bit size which ranges from 8 to 12 inches, and logging tools designed to operate within that range. But the well's diameter

may be larger or smaller than bit size due to wash out, or the collapse of shale and build-up of mud cake on porous and permeable formations. However, a large diameter will be beyond the reach of some devices and the tools will read the mud values (Asquith and Gibson, 1982). In the case of a small diameter, it would spring from high to low values due to the intermittent contact with the borehole wall (Opuwari, 2010)

Drilling mud Drilling mud helps remove cutting from the well bore, cool the drill bit, and its most important role, to prevent blow-out by keeping hydrostatic pressure of the mud column greater than formation pressure. The difference in pressure will force some of the mud to invade porous, permeable formations, and flush out the original formation fluids. In such an instance the shallow depth of the investigation tools would not reflect original formation properties. Cold mud would disturb the formation temperature by cooling it gradually as the mud circulates. In this study environmental corrections were applied to gamma ray, density, and resistivity logs using mud/borehole properties identified from log headers.

UNIVERSITY of the
WESTERN CAPE

Gamma ray The gamma ray log measures the total natural gamma radiation emanating from a formation. Once gamma rays are emitted from the source it reduces in energy as result of collision with any non-zero density object (Lehmann, 2010), hence drilling mud attenuate gamma rays produced by the formation. Large diameter holes will show more attenuation to the gamma rays because of the additional amount of mud between the formation and gamma ray detector.In this study corrections have been carried out for drilling mud, and hole diameter using mud density and caliper log as input parameters. Figure 4.1 shows an example of an uncorrected gamma ray log and environmentally corrected log for FN-12. The green curve is the uncorrected gamma ray log, while the green curve is the corrected one.

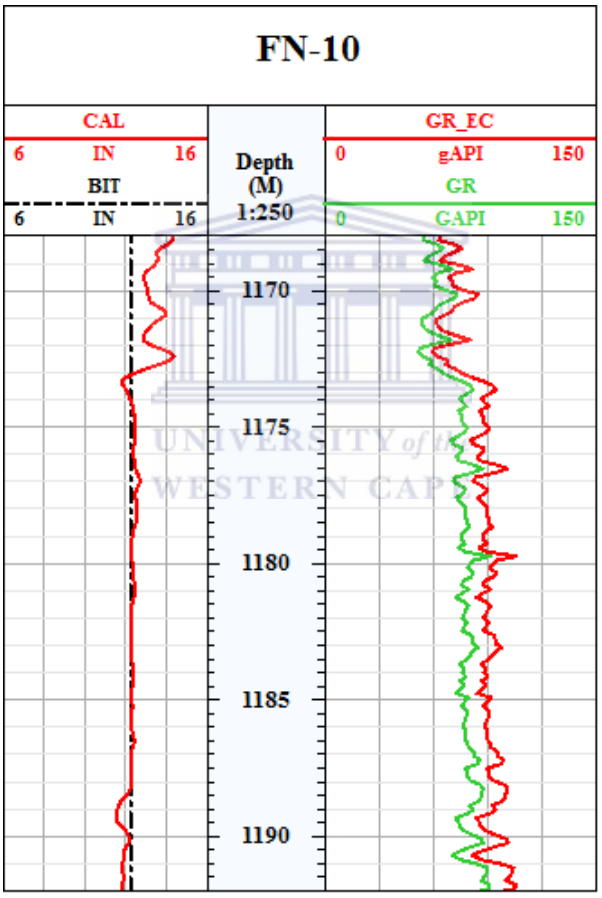

Figure 4.1: Graphics of uncorrected (green) and environmentally corrected gamma ray logs(red)

Density The formation density log measures the bulk density of the formation. The formation density tools are induced radiation tools. They emit gamma rays in the formation and measure how much radiation returns to a detector. The tool normally runs eccentered, and has a shallow depth of investigation, thus it is affected by a rough borehole wall. Additionally drilling mud reduces the radiation that returns to the detector (Glover, 2013). Figure 4.2 is an example of an uncorrected density log (blue) and environmentally corrected log (red) for FN-12.

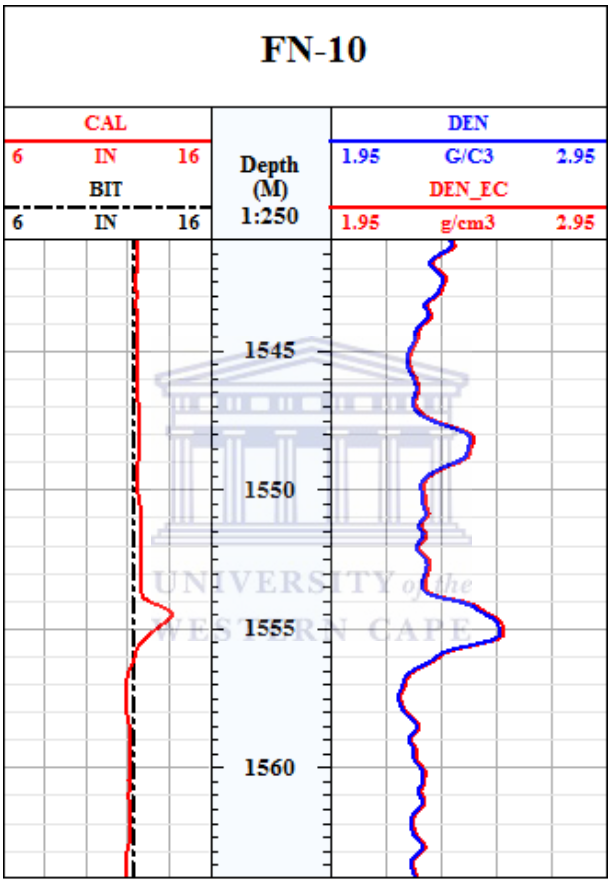

Figure 4.2: Graphics of uncorrected (blue) and environmentally corrected Density logs(red)

Resistivity Resistivity tool measures the formation resistivity, but the process of drilling actually disturbs the formations surrounding the borehole through the process of invasion, due to the replacement of formation water by mud filtrate; thus measured values need to be corrected for mud resistivity. Mud resistivity at any point along the borehole is calculated using the mud sample resistivity from the LAS file header and formation temperature at that point. Figure 4.3 shows an example of an uncorrected resistivity log (red) and environmentally corrected log (blue) for FN-12.

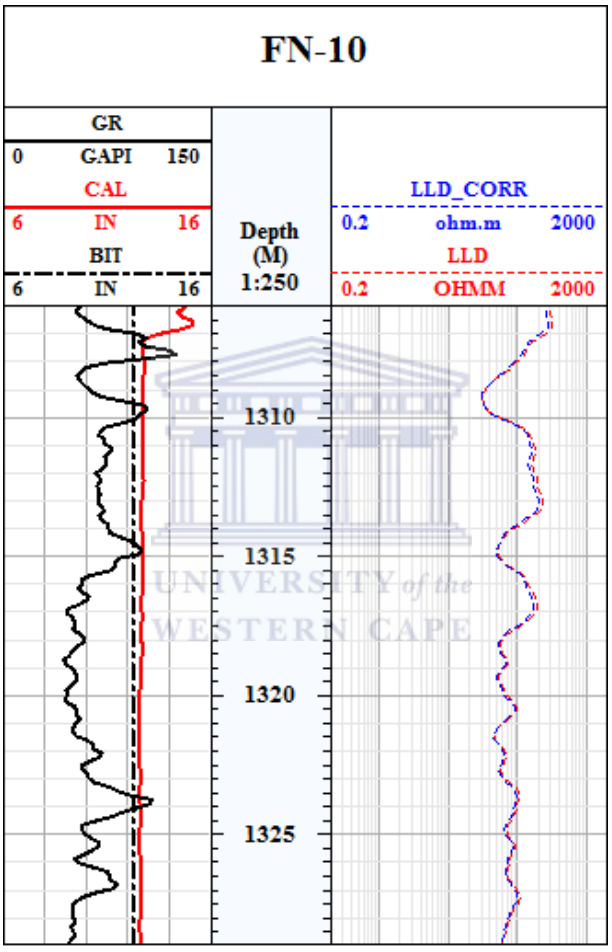

Figure 4.3: Graphics of uncorrected (red) and environmentally corrected resistivity logs (blue).

4.1.1.2 Log Normalization

'Normalization generally occurs in compensating the log measurements for one or more conditions; including inaccurate tool calibration, "drift" in the measuring devices, differences in tool response resulting from differences in tool types, differences in rock and fluid properties, the relative angle between borehole and formation, and anisotropy in order to adjusts for differences among data from varying sources to create a common basis for comparison' (Shier, 2004).
In this project three wells were logged by Sclumberger while well FN-92 was logged by China National logging Corporation (CNLC). Hence normalization had to be done to account the difference in tool type.

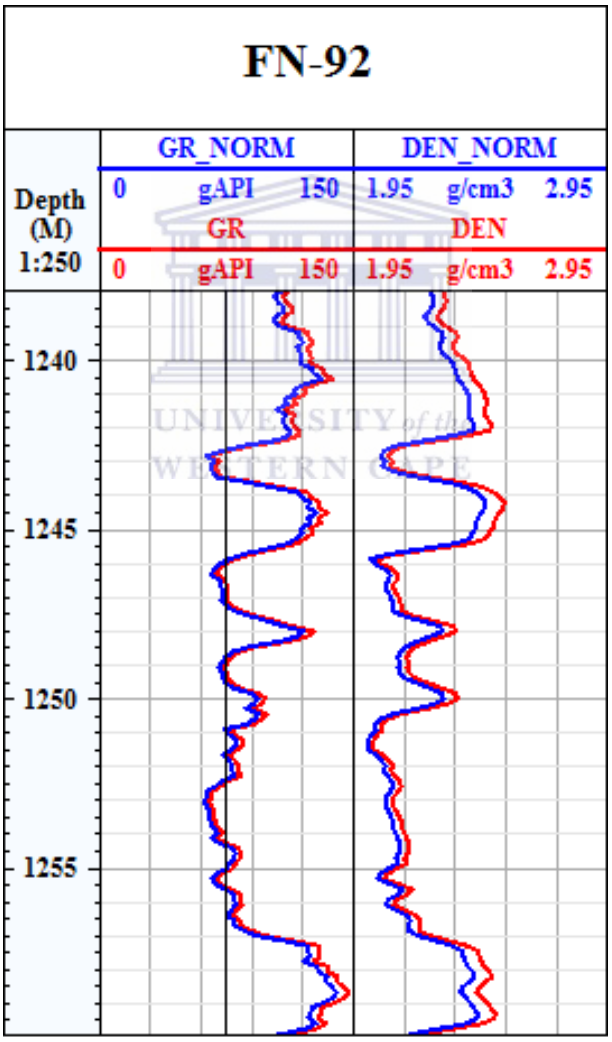

Figure 4.4: Graphics of normalized gamma ray and density logs for FN-92.

4.1.2 Core data

Core data from well FN-12 was provided for this project, including five cuts intermittently within the interval from 1172.75- 1321.48 meters with 77.25% as the average recovery rate. The core data utilized include conventional and special core analysis. Cored intervals are shown in the table below

Table 4.1: FN-12 cored intervals

Core number	Interval cut (meter)	Interval recovered (meter)	Meter recovered	Percentage recovered	
1	1172.75 - 1176.64	1172.75 - 1176.25	3.51	90.23	
2	1241.50 - 1244.24	1241.50 - 1243.72	2.2	81.02	
3	1244.24 - 1248.14	1244.24 - 1245.87	1.63	41.8	
4	1273.92 - 1277.80	1273.92 - 1276.80	2.88	74.23	
5	1317.61 - 1321.48	1317.61 - 1321.44	3.83	98.97	

4.1.2.1 Conventional core analysis

Measurements include permeability; porosity, fluid saturation, gamma ray, as well as lithology description were available from the conventional core analysis. Those core measurements were digitized and entered into spreadsheet database for processing. For the raw conventional core measurements see Appendix A.

4.1.2.2 Special core analysis

Special core analysis measurements included Archie exponents (M and N), and porosity at the overburden pressure. A total of twenty four samples were selected for special core analysis. Ten samples were selected for M and N measurements, in this project the average of the measurements were used later in saturation calculation. The M and N measurements are shown in table 4.2 and 4.3 respectively.

Table 4.2: Measurement saturation exponent from selected samples

Sample number	Depth	M	Sample number	Depth	M
21	1275.45	1.64	41	1319.17	1.91
24	1276.19	1.54	54	1320.66	1.78
27	1276.6	1.8	57	1320.87	1.81
29	1317.7	1.8	62	1321.24	1.68
32	1318.17	1.9	64	1321.41	1.78

Table 4.3: Measurement cementation exponent from selected samples

Sample number	Depth	N	Sample number	Depth	N
21	1275.45	1.71	41	1319.17	1.95
24	1276.19	1.6	54	1320.66	1.8
27	1276.6	1.85	57	1320.87	1.83
29	1317.7	1.81	62	1321.24	1.76
32	1318.17	1.92	64	1321.41	1.82

4.1.2.3 Porosity correction

Conventional core analysis porosity values were measured at room conditions; hence a need for in-situ conditions corrections, which are available at special core analysis. To do so, uncorrected porosities were plotted against porosities that measured at overburden pressure to obtain the relationship between corrected and uncorrected porosities. Corrected and uncorrected core porosities are tabulated in table 4.4.

Table 4.4: Corrected and uncorrected core porosities for FN-12

Depth	Uncorrected Porosity	Corrected Porosity
1275.45	26.5	23.8
1276.19	10.4	9.4
1276.60	35.9	31.2
1317.70	30.2	24.5
1318.17	31.6	26.4
1319.17	30.1	24.7
1320.66	22.6	19.1
1320.87	24.9	20.6
1321.24	35.0	30.3
1321.41	21.9	19.2

$$\text{correctedporosity} = 0.7836346 * \text{UncorrectedPorosity} + 2.172275 \tag{4.1}$$

4.1.2.4 Core-Log Depth Matching

Core data normally used to validate well logs derive petrophysical parameters. The depth of each set of data is identified by different providers at different times. This indicates the difference between wireline depth (log depth) and drill depth (core measurements depth). Thus, for reliable calibration between petrophysical parameters obtained from logs, with those obtained from core data, depth must be consistent between logs and core data.

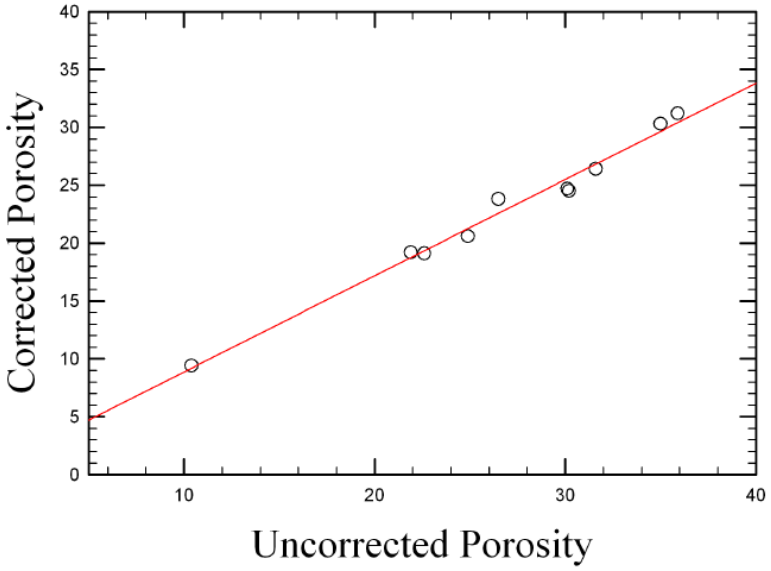

Figure 4.5: Uncorrected core porosity and corrected core porosity relationship for FN-12

Shifted core depths are tabulated in table (4.5).

Table 4.5: Core-log depth shift for E-BB1 and E-AO1 wells.

Well	Core	Cored Interval (m)		Corrected Interval (m)		Shift
		Top	Bottom	Top	Bottom	
FN-12	1	1172.75	1176.25	1173.85	1177.35	1.1
FN-12	2	1241.56	1243.72	1243.35	1245.51	1.79
FN-12	3	1244.31	1245.75	1246.68	1248.12	1.79
FN-12	4	1273.95	1276.75	1276.32	1279.12	2.37
FN-12	5	1317.61	1321.44	1318.92	1322.75	1.31

4.1.3 The Concept of Artificial Neural Networks; application in Facies and water saturation determination from logs.

Reservoir characterization is the process in which quantities of the formation properties such as porosity, permeability, and water saturation are determined. The determination of these properties is usually followed by reservoir modeling and simulation. However, to determine the aforementioned formation properties, integration of all the available data is needed for the most reliable and accurate outcomes. Well logs record vertical continuous information about the subsurface formation as a subsequent response to the signals that are being sent to the formation. The analysis outcome of the responses will come up with the formation properties needed to be determined to characterize the reservoir. The calculation of the formation properties assumes a linear or modeled nonlinear relationship

that is sufficient for modeling between the rock properties and well log responses. Other assumptions that limit the applicability of these calculations are constant or uniformly distributed grain density, and constant formation water resistivity, which has huge uncertainty (Mohaghegh et al., 1996). Thus the estimation of reservoir properties from conventional log analysis in formations where the spatial distribution of the properties such as grain density and water resistivity is non-uniform and non-linear is difficult, and complex to the extent that cannot be solved by conventional methods (Lim, 2005). An artificial neural network is a biologically inspired computing methodology with the ability to learn by mimicking the method used in human brain . An artificial neural network does not use algorithmic processes. They respond, like humans, to things learned by experience. Therefore it is necessary to expose the network to sufficient examples or training patterns, thus it can adapt and learn from the start of processing. This adaptation or learning is based on pattern recognition, by classifying new patterns and predicting an output based on the learned patterns. Thus making neural networks well suited to complex problems (Aminian and Ameri, 2005). "Patterns recognition are considered as one of the artificial neural networks strong points. The importance of pattern recognition is the processing of parallel information at the same time, the parallel distribution of information through the networks accommodates this importance. Artificial neural networks are relatively insensitive to data noise, as they have the ability to determine the underlying relationship between model inputs and outputs, resulting in good generalization ability" (Gharbi and Mansoori, 2005). Recent advances in neural networks have provided computers with the significant ability to produce a reasonable result to problems that are difficult to be solved by formal logical means. Even in the cases where the input information is noisy and less accurate (Ali, 1994).

4.1.3.1 Facies distribution

Facies refers to the sedimentary rocks with the same lithological, physical, and biological attributes relative to all adjacent deposits (Octavian, 2006) . It reflects similar physiochemical conditions in their environment, even if they are of different ages (Serra, 1985). To achieve an accurate formation evaluation using petrophysical parameters such as porosity and water saturation, one must account for the variation of petrophysical properties within the reservoir which is mostly controlled by facies distribution (Yumei, 2006; Dubois et al., 2007). Hence this study aims to identify the subsurface facies distribution across the reservoir to get reliable estimation for the petrophysical parameters. Facies could be generated from wireline logs using either an unsupervised method where the well is divided into different facies based on log behavior (Artifcial Neural Network), or a supervised method where the well is divided to different facies according to facies identified

from core description in a well or nearby well (Saggaf and Nebrija, 2000).
This thesis made use of the supervised method. Four sand facies were identified from core description

(A) Grey medium to coarse grain, poorly sorted poor to medium siliceous cemented pebbly sandstone. This facies occurs in core three (1245.3 - 1247.2).
(B) Grey fine grain, well sorted, medium siliceous cemented sandstone. This facies occurs in core one (1175.5 - 1177.1), core four (1276.3 - 1277.8) and core five (1322.8 - 1323.3).
(C). Grey very fine grain, well sorted, well siliceous cemented sandstone, this sandstone characterized by interbedded shale lamination. This facies occurs in core one (1173.3 - 1174.6) and core five (1319.8 - 11322.7).
(D). Light grey fine- grain, well sorted, well argillaceous cemented sandstone, this sandstone is highly argillaceous. This facies occurs in core one (1174.7 - 11775.4), core two (1242.8 - 1245.2), core four (1275.1 - 1276.4) and core five (1319.1 - 1319.7).

4.1.3.2 Facies from logs

Since facies cannot be identified directly from wireline log measurements and given the limitation of the core data, one has to rely on facies identification approaches which include statistical methods and artificial intelligent techniques. The statistical methods only give good results when using large amounts of data. Their performance is constrained by the number of samples and well logs (Tang and White, 2008) . Artificial intelligent techniques are computer models (or computational systems) for solving nonlinear complex problems. In this study, the artificial neural network method, in which parallel analysis is used to simulate between core and wireline data, is considered (An, 2000). The network learnt the relationships between the petrophysical properties and a pre-existing classification, such as core facies. It then clusters the input data into different groups that are internally homogeneous and externally isolated, on the basis of a measure of similarity or dissimilarity between groups (Kumar and Kishore, 2006). Once a model linking properties and facies has been learned, ANN applies the model and creates a geological facies prediction for core surrounding intervals and other wells based on indexation input.

Work flow The Ipsom module in Techlog software provides a solution to identify facies from wireline logs with both supervised and unsupervised methods. As mentioned above, the advantage of the supervised method is the integration of wireline logs and core data for a more accurate classification, since information on lithology from only wireline logs could not be sufficient (Gluyas and Swarbick, 2004) . The following combination of wireline logs is used as lithology logs according to (Qi and Carr, 2006; Gifford and Agah, 2010; Rider, 1996).

- Gamma ray log (GR)
- Deep resistivity log (ILD or LLD)
- Neutron porosity log (NPHI)
- Sonic log (DT)
- Bulk density log (RHOB)
- Photoelectric factor (PEF)

This combination of logs was loaded in the Ipsom module along with core identified facies for the indexation process. Figures 5.20, 5.21, 5.22 and 5.23 shows the core identified facies and the input logs in the cored well.

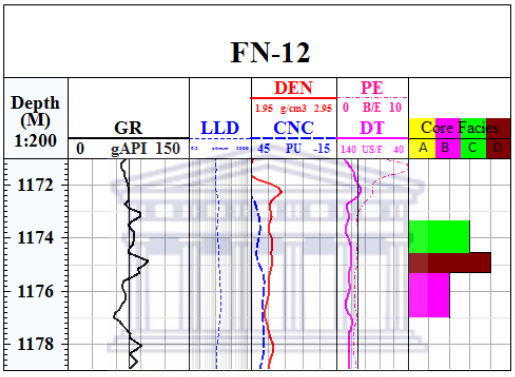

Figure 4.6: Core identified facies and the input logs in the cored well over core interval one

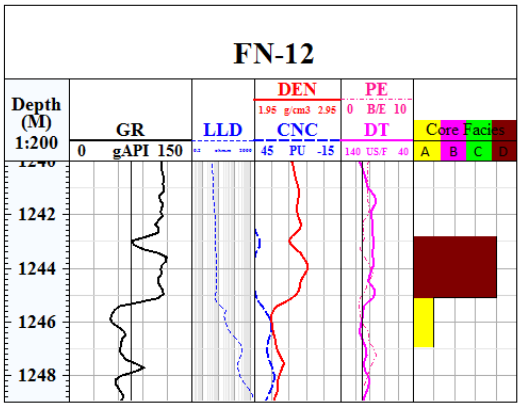

Figure 4.7: Core identified facies and the input logs in the cored well over core interval two and three

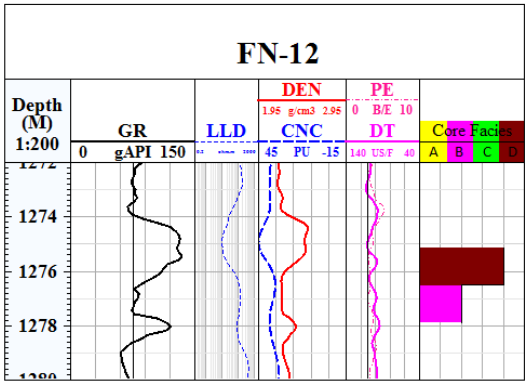

Figure 4.8: Core identified facies and the input logs in the cored well over core interval four

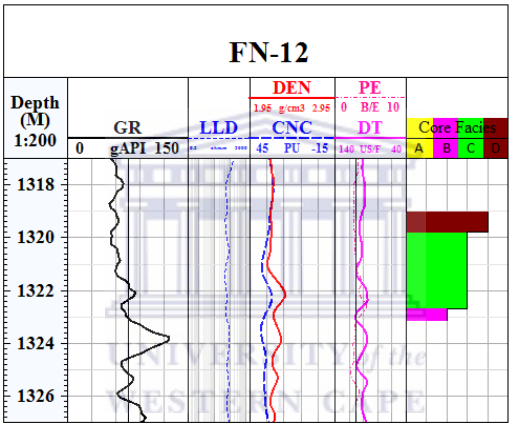

Figure 4.9: Core identified facies and the input logs in the cored well over core interval five

Results Once wireline logs and core data is loaded into Techlog, it will start the indexation process for the zones corresponding to core facies. The resulting model is then applied for all studied wells to create classification curves. Normalized maximum and minimum values for each input log has been tabulated in table (5.1). Also correlation between input logs and created classification curves was done to assess the contribution of each log, which is indicated by correlation values. Values close to one means high correlation with facies, while values close to zero means a poor correlation with facies, therefore less contribution as shown in table (5.2).

The statistic of each predicted facies is presented in table 5.3 . The number of samples is number of nodes associated to each facies.

To validate the outcome of facies predictions through this method, comparison was made between the core facies and facies that were obtained from logs. It enabled checking of

Table 4.6: Normalized minimum and maximum values for input logs of the studied wells

NO	Input log	Norm min	Norm max
1	RHOB	2.34668	2.67413
2	DT	61.0054	85.4784
3	LLD	5.0447	121.564
4	GR	37.8741	145.764
5	NPHI	0.047	0.2651
6	PEF	2.4648	4.4137

Table 4.7: The correlation factor and the contribution of each input log.

NO	Input log	Correlation	Information
1	RHOB	0.79916	0.17385
2	DT	0.4276	0.09302
3	LLD	0.88032	0.19151
4	GR	0.9332	0.20301
5	NPHI	0.8388	0.18247
6	PEF	0.71775	0.15614

Table 4.8: The statistic of predicted facies

Facies	**A**	**B**	**C**	**D**
Number of samples	595	150	294	330
Input logs	Mean	Mean	Mean	Mean
RHOB	2.171	2.2018	2.1580	2.2543
DT	107.941	113.7921	113.3478	103.4723
ILD/LLD	431.6652	217.5710	137.3077	38.9444
GR	62.9245	68.2024	80.5592	91.7785
NPHI	37.0783	38.2225	41.4106	36.5226
PEF	4.3670	3.308512	3.7841	3.324

whether the resultant model was applicable to uncored intervals and other wells or not. The correlation between the core facies and predicted facies in FN -12 is shown in figures 5.24 and 5.25. The figures indicate good consistency between core and predicted facies. detailed facies distribution within the studied reservoirs are given in chapter six

4.2 Petrophysical model

In this chapter, an integrated petrophysical model is created. The initial step is to identify the reservoir zones within which, facies distributions as well as petrophysical parameters were determined. Petrophysical parameters include shale volume, porosity, effective porosity, and water saturation. These petrophysical parameters were obtained from wireline logs using oil industry accepted formulas in Techlog 2011Â© software. The core data

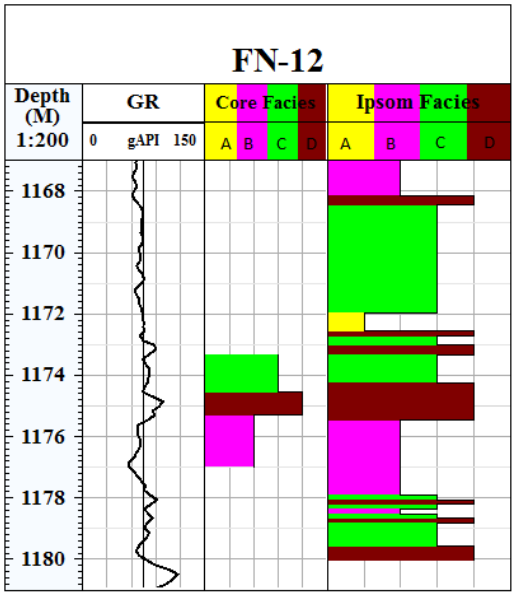

Figure 4.10: Correlation between core facies and wireline facies in FN-12, core interval one

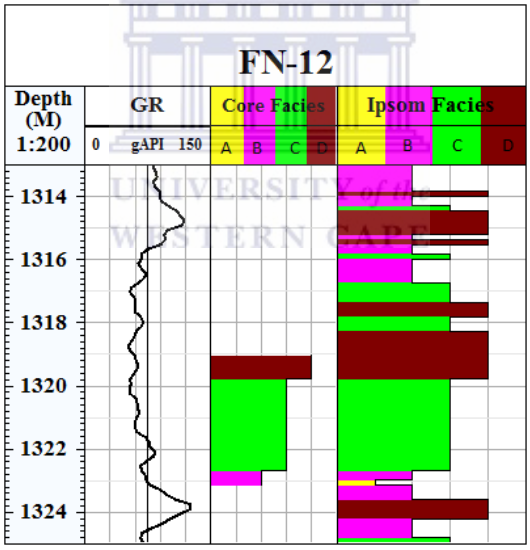

Figure 4.11: Correlation between core facies and wireline facies in FN-12, core interval five

was used to calibrate the petrophysical model to confirm the accuracy of the model.

4.2.1 Reservoir zones

The initial step in formation evaluation is to identify zones of interest or the reservoir intervals. These zones are characterized by lesser volume of shale (Amigun et al., 2012). A combination of gamma ray logs which reflects the degree of shaliness, resistivity logs which reflect the hydrocarbon saturation having known that oil has high resistivity, and

density and neutron logs to indicate if there are gas zones (concept of crossover) were used for this study (Quijada and Steward, 2007).
Five reservoir zones were identified within the studied area from the Fula north field. The first reservoir zone is associated with the Ardeiba Formation which ranges from the Turonian to late Senonian period. This formation is generally related to deposits of several fluvial/deltaic channel sands generally ranging from three to twenty one meters thick, which is an indication of a reservoir (Schull, 1988). This formation also consists of interbedded floodplain and lacustrine claystones, and shales, which are considered as a significant reservoir seal. In addition, information from the core reports state that the rest of the reservoir zones are associated with the Bentiu Formation which underlies the aforementioned formation and consists of predominantly sand units. This section is considered to be the primary reservoir of the Muglad Basin. These sandstone sequences were deposited in braided and meandering streams during the late Albain to Cenomanian period. The Bentiu Formation overlies the Aptain to early Albain Abu Gabra Formation which consists of several thousand feet of organic-rich lacustrine claystones and shales considered to be the primary source rock for the Muglad Basin (Lirong et al., 2013).

4.2.1.1 FN-12 reservoir zones

The first reservoir zone in this well ranges from 1166.6m to 1180.06m, having a thickness of 13.46m as shown in figure 5.1 below.Further, the resistivity logs suggest the invaded and uninvaded zone have a similar fluid content, because there is no separation between the deep and short resistivity logs. Furthermore, neutron and density logs (porosity logs) show no sign of crossover throughout this reservoir zone. All which Points to the likely absence of gas in the reservoir

The second zone in FN-12 is ranging from 1242.98m to 1260.38m, having a thickness of 17.4m as shown in figure 5.2. The high resistivity of the uninvaded zone, indicated by the separation between the deep and the short resistivity logs suggests that zone contains hydrocarbon. While, neutron and density logs (porosity logs) show no sign of crossover throughout this reservoir zone. That points more likely to the absence of gas in the reservoir

The third zone in FN-12 is ranging from 1275.66.2m to 1288.4m, having a thickness of 12.74m while the fourth zone is ranging from 1289.92m to 1306.7m, having thickness of 16.78m. Both zone three and four are shown in figure 5.3. For both zones the high resistivity of the uninvaded zone, indicated by the separation between the deep and the short resistivity logs suggests that the zone contains hydrocarbon. While, neutron and density logs crossover at the depth ranges from 1297.4m to 1298.4m for reservoir zone

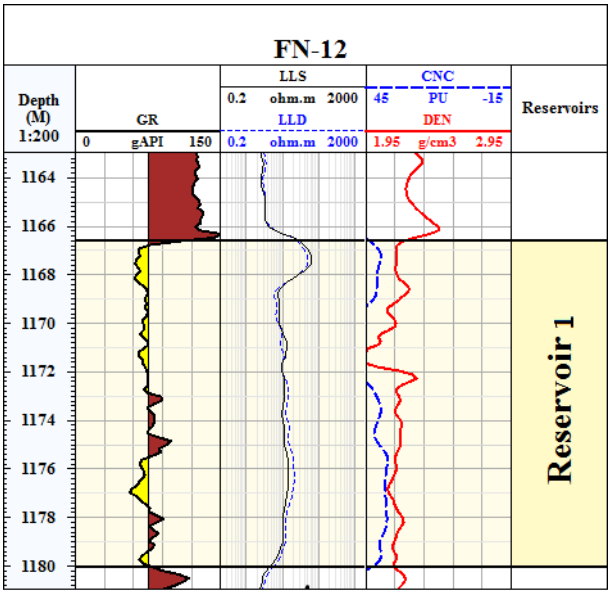

Figure 4.12: reservoir zone one in FN-12

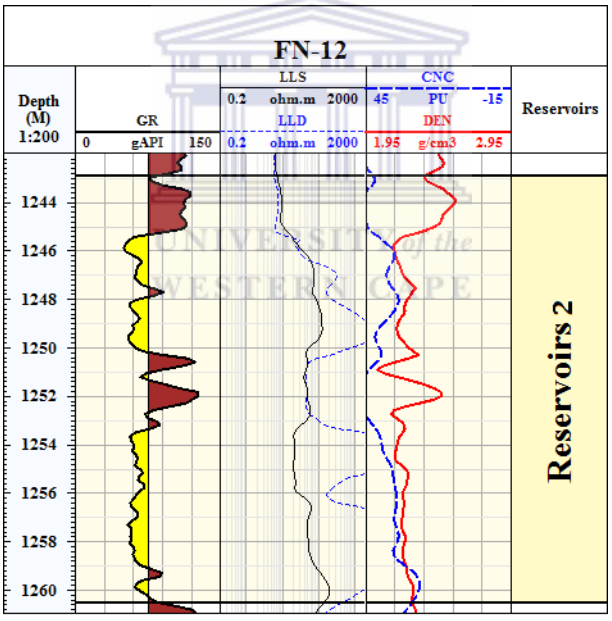

Figure 4.13: reservoir zone two in FN-12

four indicates a gas presence over the aforementioned depth.

Zone five in FN-12 is ranging from 1315.21m to 1323.16m, having a thickness of 7.95m as shown in figure 5.4. Neutron and density logs show no sign of cross over throughout this reservoir zone. This means a no gas zone is detected within this zone. Moreover, the separation between resistivity logs indicates the presence of hydrocarbon in uninvaded zone.

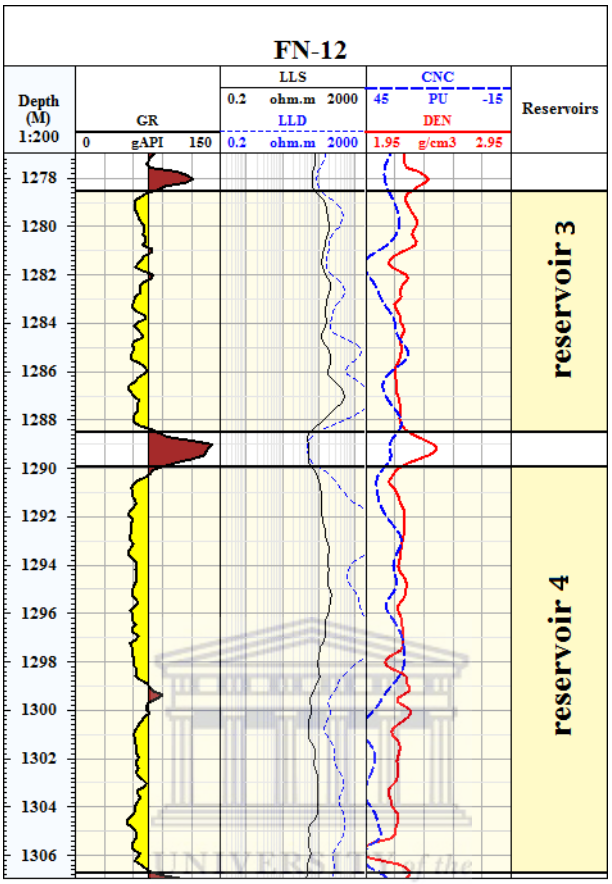

Figure 4.14: reservoir zone three and four in FN-12

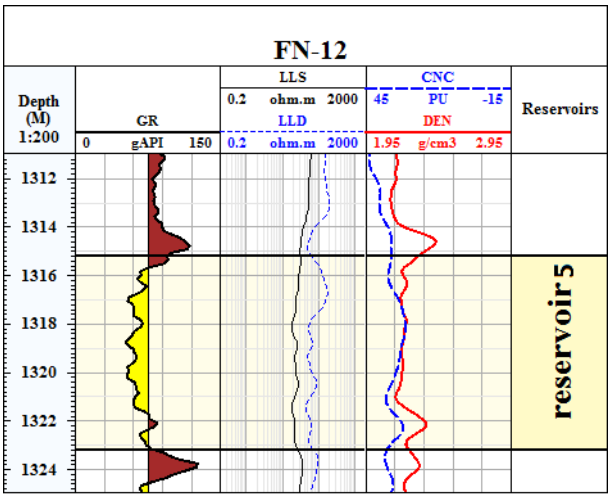

Figure 4.15: reservoir zone five in FN-12

4.2.1.2 FN-92 reservoir zones

The first zone in the well ranges from 1172.5m to 1180.85m, having a thickness of 8.35m as shown in figure 5.5. The resistivity logs suggest the invaded and uninvaded zones have a similar fluid content, because there is no separation between the deep and short resistivity. While, neutron and density logs show no sign of gas presence within this reservoir.

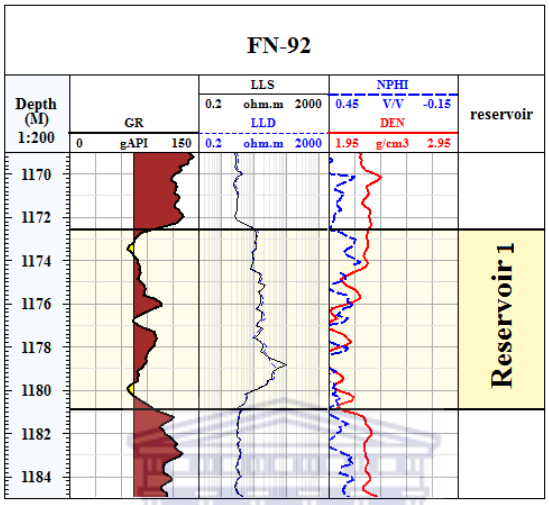

Figure 4.16: reservoir zone one in FN-92

The second zone in this well is ranges from 1245.62m to 1257.04m, having a thickness of 11.42m as shown in figure 5.6. The resistivity logs suggest that the invaded and uninvaded zones have a similar fluid content up to depth 1252m, but from the aforementioned depth up to 1257m the fluid content differs between the invaded and uninvaded zone. Moreover, the behavior of porosity logs indicate a gas zone ranges from 1248.4m to 1248.8m.

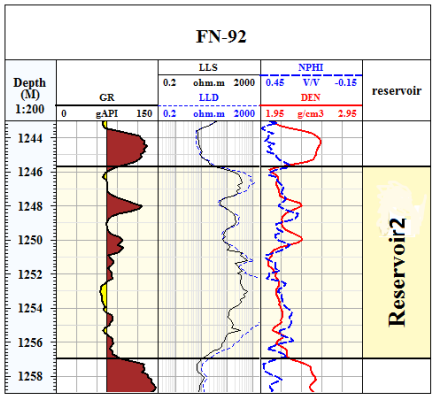

Figure 4.17: reservoir zone two in FN-92

The third zone in the well ranges from 1278.88m to 1286.57m, having a thickness of 7.69m as shown in figure 5.7. The resistivity logs suggest different fluid content between the invaded and uninvaded zones. While the crossover between porosity logs at depth from 1285.4m to 1286.2m indicates the presence of gas at that depth

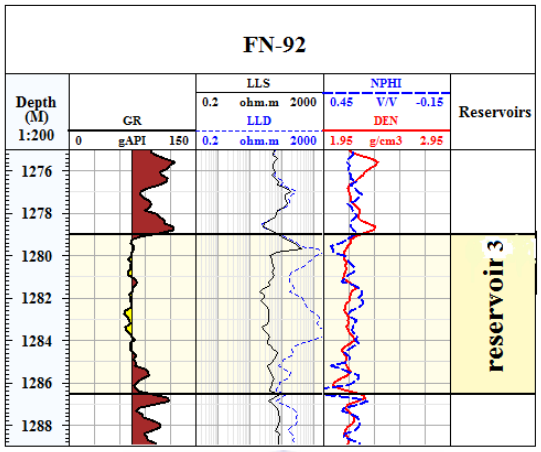

Figure 4.18: reservoir zone three in FN-92

The fourth zone in the well ranges from 1296.21m to 1309.91m, having a thickness of 13.7m as shown in figure 5.8. Resistivity logs suggest a different fluid content between the invaded and uninvaded zones. While the behavior of porosity logs suggests the presence of gas zones in the upper part of the reservoir up to a depth of 1303.2m.

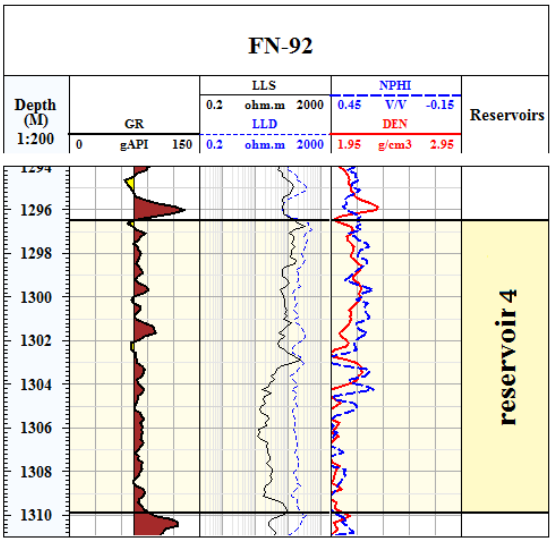

Figure 4.19: reservoir zone four in FN-92

The fifth zone in the well ranges from 1314.1m to 11324.07m, having a thickness of 9.97m as shown in figure 5.9. The resistivity logs suggest the invaded and uninvaded zones have a similar fluid content, because there is no separation between the deep and short resistivity. Furthermore, porosity logs show no sign of crossover throughout the reservoir zones. Thus, no gas zone is detected throughout the reservoir

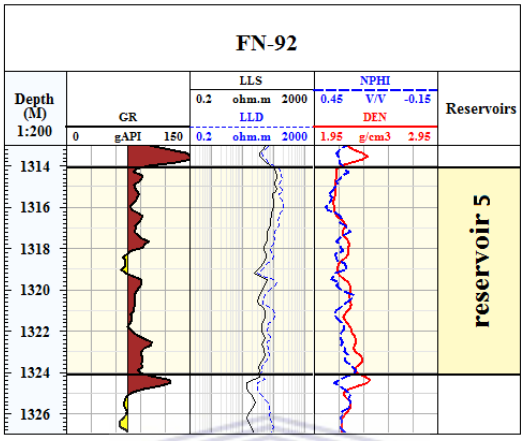

Figure 4.20: reservoir zone five in FN-92

4.2.1.3 FN-10 reservoir zones

The first zone in the well ranges from 1159.74m to 1173.37m, with a thickness of 13.63m as shown in figure 5.10. The resistivity logs suggest the invaded and uninvaded zones have a similar fluid content, because there is no separation between the deep and short resistivity. Furthermore, detecting gas zones in this reservoir is not possible due to the lack of neutron log measurements.

The second zone in the well ranges from 1235.17m to 1253.97m, having a thickness of 18.8m as shown in figure 5.11 below. The resistivity logs suggest the invaded and uninvaded zones have a similar fluid content, because there is no separation between the deep and short resistivity.

The third zone in the well ranges from 1264.58m to 1277.43m, with a thickness of 12.58m as shown in figure 5.12. The resistivity logs suggest that the invaded and uninvaded zones have a similar fluid content, because there is no clear separation between the deep and short resistivity.

The fourth zone in the well ranges from 1282.42m to 1302.27m, having a thickness of 19.85m as shown in figure 5.13. The resistivity logs suggest the invaded and uninvaded

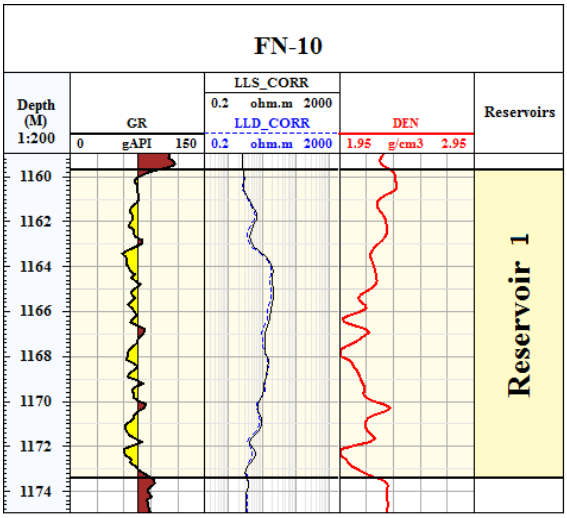

Figure 4.21: reservoir zone one in FN-10

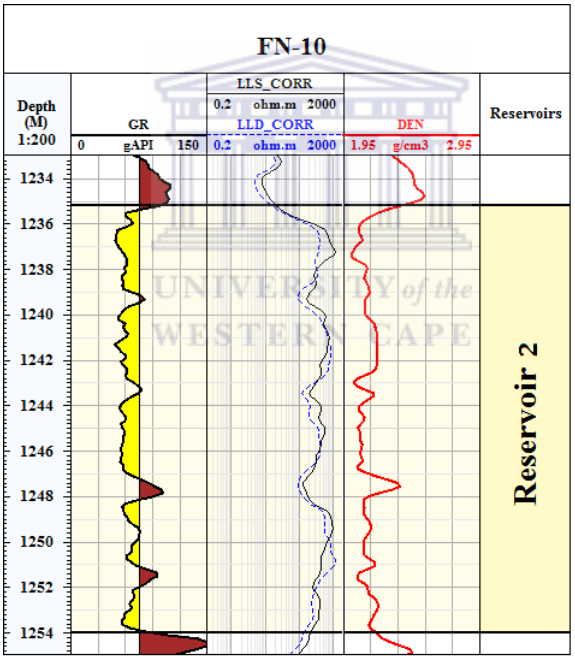

Figure 4.22: reservoir zone two in FN-10

zones have a similar fluid content at the upper part of the reservoir up to a depth of 1286m, while different fluid content can be observed at the lower part of the reservoir.

The fifth zone in the well ranges from 1308.04m to 1321.18m, with a thickness of 13.14m as shown in figure 5.14. The resistivity logs suggest that the invaded and uninvaded zones have a similar fluid content, because there is no clear separation between the deep and short resistivity.

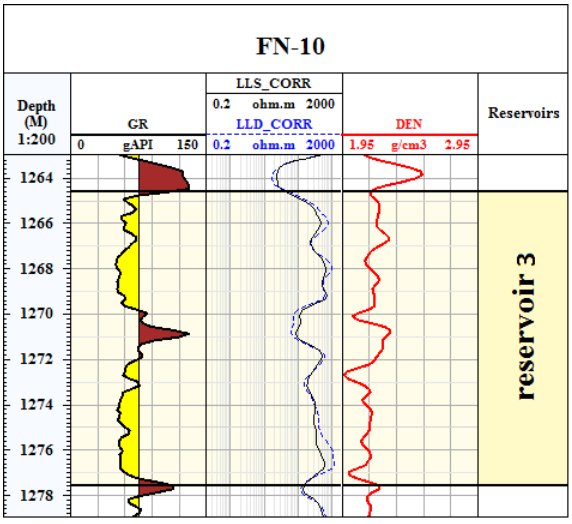

Figure 4.23: reservoir zone three in FN-10

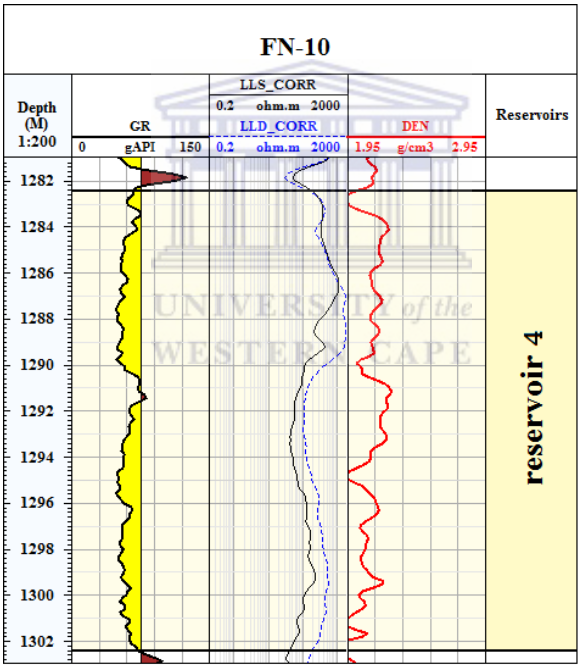

Figure 4.24: reservoir zone four in FN-10

4.2.1.4 FN-94 reservoir zones

The first zone in the well ranges from 1172.86m to 1180.48m, having a thickness of 7.62m as shown in figure 5.15. The resistivity logs suggest that the invaded and uninvaded zones have a similar fluid content, because there is no separation between the deep and short resistivity. While the porosity logs crossover indicates a gas zone range from 1175m to 1176.2m.

The second zone in the well ranges from 1244.58m to 1254.33m, with a thickness of 9.75m

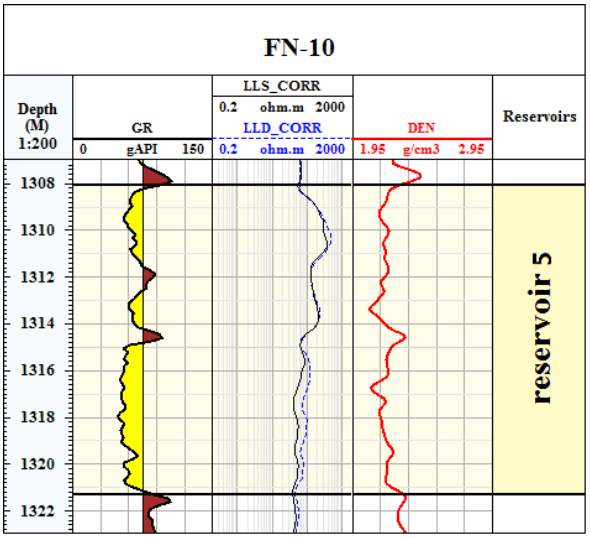

Figure 4.25: reservoir zone five in FN-10

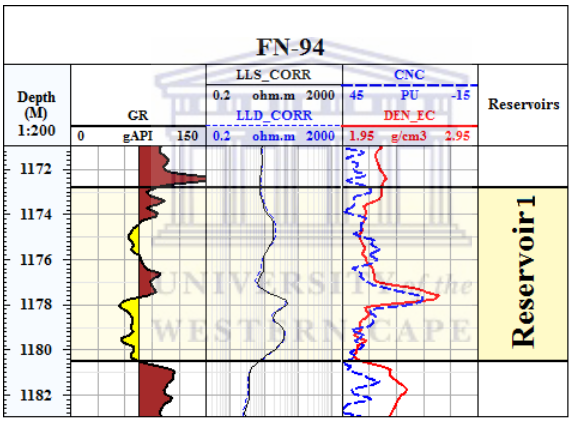

Figure 4.26: reservoir zone one in FN-94

as shown in figure 5.16. The resistivity logs suggest that the invaded and uninvaded zones have a similar fluid content, because there is no separation between the deep and short resistivity. Furthermore, the abrupt decrease in the density log over depth 1247.2m to 1248.4m indicates a gas presence due to the crossover with the neutron log

The third zone in the well ranges from 1277.05m to 1286.28m, having a thickness of 9.23m as shown in figure 5.17.Different fluid content between the invaded and uninvaded zones over depths from 1278m to 1280m, and 1281m to 1285m can be observed fromthe resistivity logs separation. The porosity logs suggest a gas zone range from 1277.9m to 1279.4m.

The fourth zone in the well ranges from 1294.18m to 1312.94m, having a thickness of 18.76m as shown in figure 5.18. Resistivity logs suggest a different fluid content through

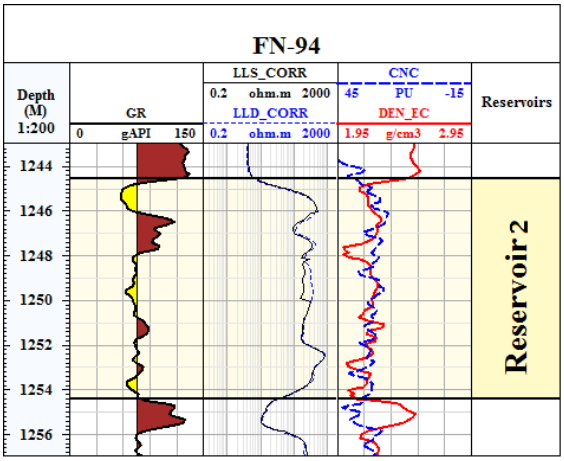

Figure 4.27: reservoir zone two in FN-94

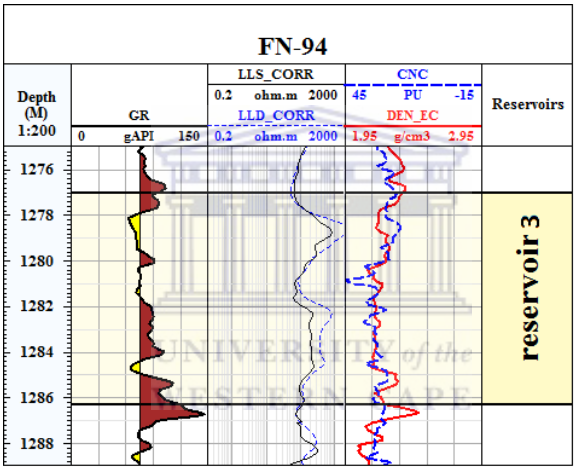

Figure 4.28: reservoir zone three in FN-94

the reservoir. Moreover, the logs suggest gas absence through the reservoir interval.

The fifth zone in this well is ranging from 1322.44m to 1338.52m, having thickness of 16.08m as shown in figure 5.19. A different fluid content between the invaded and uninvaded zones over a depth from 1326m to 1330m, and 1332m to 1338.52m can be observed from the resistivity logs separation. Here too the porosity logs suggest an absence of gas through the reservoir interval.

4.2.2 Shale volume

One of the essential steps in formation evaluation is to calculate the volume of shale per unit volume of reservoir rock. Shale affects logging tool responses, and thus the volume of shale determination is critical due to its further influence on the calculation of porosity

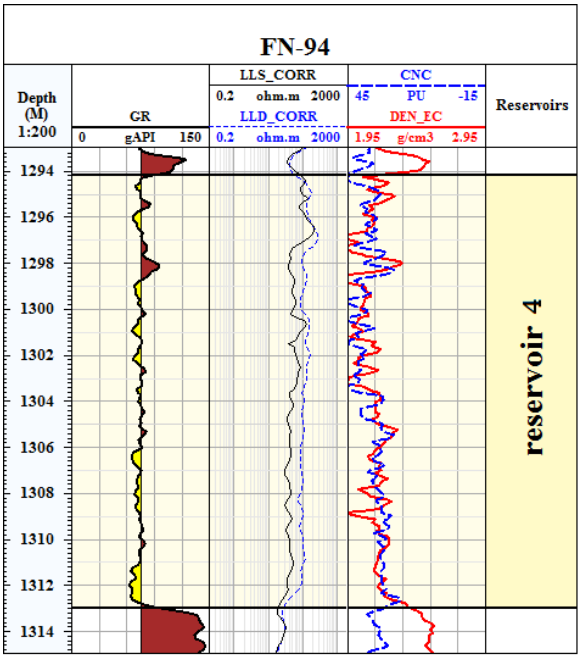

Figure 4.29: reservoir zone four in FN-94

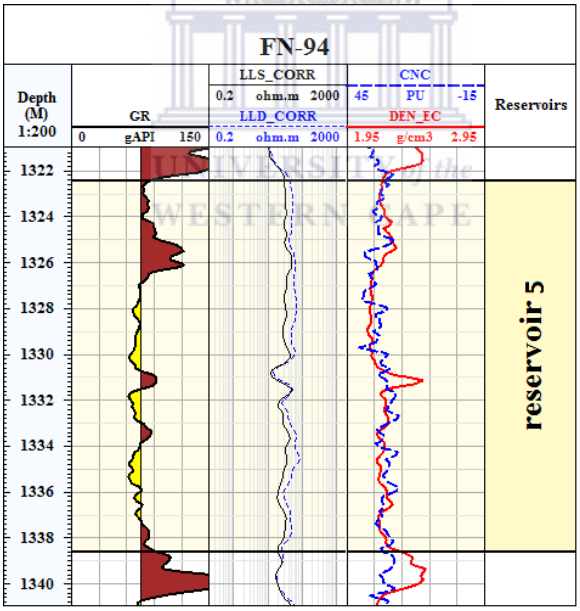

Figure 4.30: reservoir zone five in FN-94

and fluid content (Adeoti et al., 2009) .Thus if one does not account for the presence of shale the given porosity values will be optimistic, in the case of all porosity logs (neutron, sonic, and density). With the only pessimistic case occurring when using density log, with the shale density greater than the reservoir matrix density (Kamel. and Mabrouk., 2003). Also, The presence of shale tends to reduce the resistivity of formation and leads to high values of water saturation. Thus an underestimated hydrocarbon potential (Bassiouni,

1994) . Shale affects the measurements of every logging tool to some degree, hence shale volume can be determined via several log-derived clay content indicators include, single logs such as gamma ray, resistivity, and self-potential or a combination of two logs such as density-neutron, and neutron-acoustic.
In this study, gamma ray and resistivity logs have been used to determine the volume of shale.

4.2.2.1 Gamma ray shale volume

The gamma ray log measures the total natural gamma radiation emanating from a formation. Given the fact that shale is more radioactive than sand, gamma ray can be used to distinguish between shale and sand. The first step to determine shale volume from gamma ray is calculating the gamma ray index. In which the maximum gamma ray response is taken as the shale point, and the minimum response as the clean sand, the gamma ray index could then be calculated using the following formula

$$I_{gr} = \frac{GR_{log} - GR_{min}}{GR_{max} - GR_{min}} \tag{4.2}$$

where:
I_{GR} : gamma ray index
GR_{log} : gamma ray log reading in zone of interest
GR_{min} : gamma ray log reading in 100% clean zone
GR_{max} : gamma ray log reading in 100% shale
The gamma ray and resistivity sand and shale points for all studied wells are listed in table (5.4)
The shale volume was calculated using the linear method in which the volume of shale is equal to the gamma ray index.

Table 4.9: The minimum and maximum values of gamma ray logs (GR)and resistivity logs (ILD/LLD) used in shale volume calculations.

well		FN-12	FN-92	FN-10	FN-94
Resistivity	Min	2.1	1.9	1.8	1.9
	Max	577	468.7	507.7	331.3
GR	Min	32.6	36.1	30.8	36.4
	Max	139.5	143	136.9	149

4.2.2.2 Shale volume correction

Corrections proposed by (Clavier et al., 1971) and (Steiber, 1973) to calculate shale volume using the gamma ray index were carried out in this project to obtain the most reliable

results. Nonlinear formulas developed for different geologic ages were found to be more reliable.

(Clavier et al., 1971) relationship is:

$$V_{sh} = 1.7 - \sqrt{3.38 - (I_{GR} + 0.7)^2} \tag{4.3}$$

(Steiber, 1973) relationship is:

$$V_{sh} = \frac{I_{GR}}{3 - 2I_{GR}} \tag{4.4}$$

4.2.2.3 Resistivity shale volume

Depending on the lithology resistivity log, contrast is normally seen, thus shale volume could be calculated depending on that contrast, resistivity decreases as shale volume increases due to shale conductivity (Hamada, 1996). The calculation of shale volume then can be done using the following formula

$$V_{sh} = \frac{\log R_t - \log R_{ma}}{\log R_{sh} - \log R_{ma}} \tag{4.5}$$

where:
R_t : True resistivity (Resistivity log reading in zone of interest).
R_{sh} : Resistivity log reading in 100% shale.
R_{ma} : Resistivity log reading in 100% matrix rock.

4.2.2.4 Final shale volume

It is usual to select the lowest value as final shale volume at any level in the whole interval (Worthington, 1985). Calibration between different estimates of shale volume as well as the final shale volume is shown in figure 5.26.

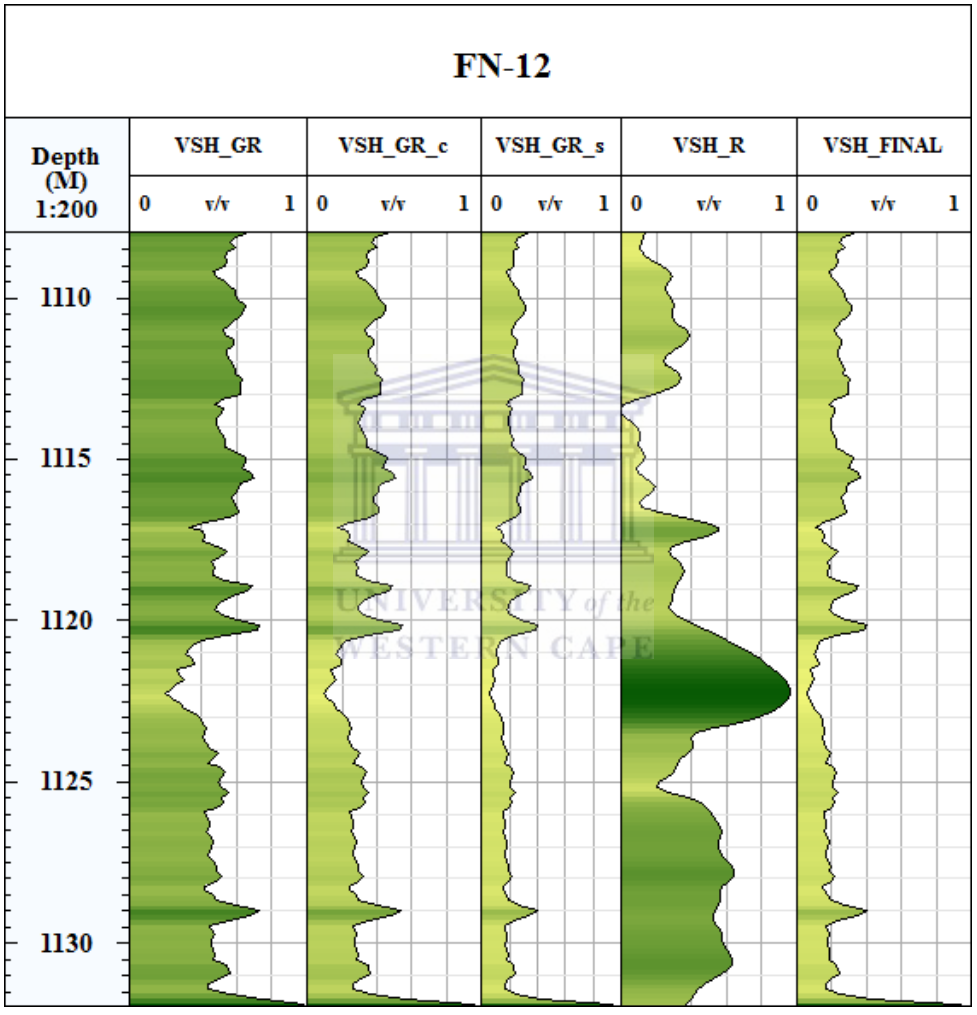

Figure 4.31: Shale volume calculation by using GR, GR Clavier et al, GR Steiber, resistivity, and final volume of shale in FN-12 from depth 1108m to 1132m

4.2.3 porosity determination

Porosity is the fraction of the volume of space between the solid particles of the rock to the total rock volume (Glover, 2013). This gives information about the possible volume of fluids within the formation. It can be expressed using the following formula.

$$\text{Porosity } (\Phi) = \frac{\text{Volume of the pore spaces}}{\text{Total volume of rock}} \tag{4.6}$$

Porosity can be expressed either as a fraction or percentage, and classified according to its geological origin into primary porosity, which developed during the sedimentation process, and porosity which developed due to diagenesis. Porosity can also be classified according to its connectivity into total porosity, which is defined as the fraction of the total pore space to the total volume of the rock, and effective porosity, which is defined as a fraction of the interconnected pore space to the total volume of the rock . Porosity can be derived from single log such as density, sonic and neutron or combination of logs such as (density-neutron) or (neutron - sonic). In this study, porosity has been obtained using density log because of the availability of core grain density values from the well report. Core grain density represent ground truth information, hence, porosity determined by this method is accurate. Porosity can be derived from single log such as density, sonic and neutron or combination of logs such as (density- neutron) or (neutron- sonic).In this study, porosity was obtained using the density log due to the availability of core grain density values from the well report. Core grain density represents ground truth information, hence, porosity determined by this method is accurate.

4.2.3.1 Density porosity

The formation density log measures the bulk density of the formation. The formation density tools are induced radiation tools. They emit gamma rays in the formation and measure how much radiation returns to a detector. The degree of return gamma rays attenuation reflects the formation density. Hence the effect on emitted gamma rays is caused by the combination of the matrix component of the formation, and the fluids occupying the pore spaces (porosity). Porosity can be calculated from density log using the following formula

$$\Phi = \frac{\rho_{\text{ma}} - \rho_{\text{b}}}{\rho_{\text{ma}} - \rho_{\text{f}}} \tag{4.7}$$

where:

Φ : the porosity of the rock.

ρ_b : the bulk density of the formation.
: the density of the rock matrix.
ρ_f : the density of the fluids occupying the porosity.

The term matrix density ρ_{ma} in the above formula, refers to the density of the solid material of the formation without the pores. Therefore to obtain reliable estimates of density porosity, formation matrix density should be determined accurately. In this project to obtain accurate input values of the matrix density, average core grain density against each facies was calculated and used as an input value for each facies interval. Calibration between core porosity and density porosity for the well FULA NORTH-12 is shown in figure (5.27).

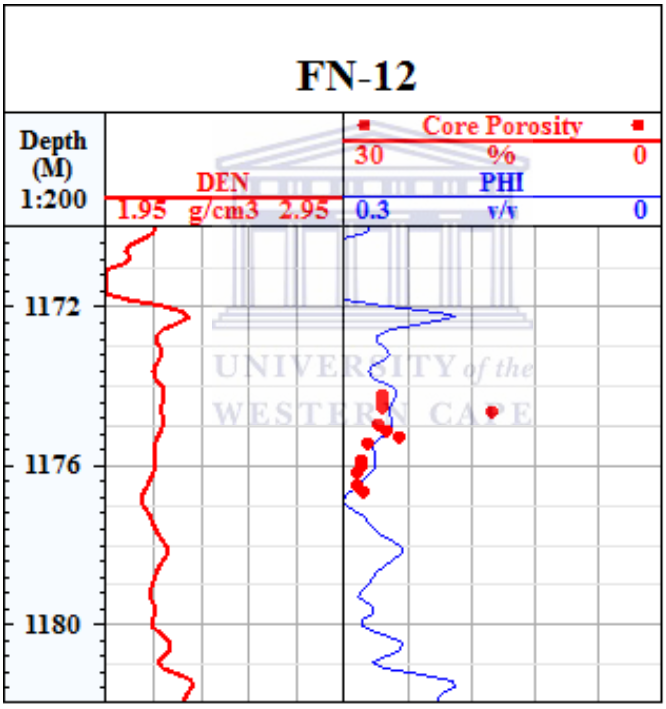

Figure 4.32: Correlation between core porosity and density porosity in FN-12

4.2.4 Effective porosity

Effective porosity is the total porosity less all the bound water associated with clays (Ellis and Singer, 2008). This means that the effective porosity approaches the total porosity in clean sand formations, while it approaches zero in shaly formations.
In this project effective porosity has been determined from density log using the following formula

$$\Phi_e = \Phi_T - (\Phi_{sh} * V_{sh}) \tag{4.8}$$

where:
Φ_e : Effective porosity.
Φ_T : Total porosity.
Φ_{sh}: Shae porosity.
V_{sh} : Shale volume.

given that:

$$\Phi_{sh} = \frac{\rho_{ma} - \rho_{sh}}{\rho_{ma} - \rho_f} \tag{4.9}$$

4.2.5 Saturation determination

The pore spaces in subsurface rocks that form a hydrocarbon reservoir should be completely saturated with water, oil and/or gas. During the deposition, reservoirs are fully saturated with water. This 100% water saturation is then reduced by oil and gas coming from adjacent source rock. This would then replace water even though the water is denser than hydrocarbons (oil and gas). Given the fact that all fluid saturations should add up to unity, hydrocarbons saturation may be determined as soon as water saturation is obtained. Water saturation is normally defined as the pore volume fraction of the reservoir rock that is filled with water. From a petrophysics point of view, water saturation is of great importance because a reliable estimation of water saturation is the key parameter to calculating the hydrocarbon volume in a specific reservoir. In this project five theoretical models were used to calculate water saturation from the well logs, followed by calibration to determine the most consistent model in the specific zone. Since these models are not universal but only fit to local data. Before the evolution of the shaly sand models, formation water used to be considered as only conductive component in the subsurface rock. Therefore Archi formula is considered to be the basic equation for calculating the water saturation in subsurface formation. From which shaly sand models have been derived. Equations of Archie as well as shaly sand models used in this project are tabulated in table (5.5)

Table 4.10: Water saturation equations used in the study.

No	Model	Equation
1	Archie	$S_w = \left(\frac{a*R_w}{R_t*\Phi^m}\right)^{\frac{1}{n}}$
2	Total shale	$S_w = \left[\frac{aR_w}{\Phi_e^2*R_t} + \left[\frac{aR_wV_{sh}}{2\Phi_e^2R_{sh}}\right]^2\right]^{0.5} - \frac{aR_wV_{sh}}{2\Phi_e^2R_{sh}}$
3	Indonesia	$\frac{1}{\sqrt{R_t}} = \left[\frac{V_{sh}^{(1-\frac{V_{sh}}{2})}}{\sqrt{R_{sh}}} * \frac{\Phi_e{}^{\frac{m}{2}}}{\sqrt{aR_w}}\right] * S_w^{\frac{n}{2}}$
4	Juhasz	$\frac{1}{R_t} = \left[\frac{\Phi^m*S_w^n}{aR_w}\right] * \left[1 + Bn * Q_{vn}\frac{R_w}{S_w}\right]$
5	Dual water	$\frac{1}{\sqrt{R_t}} = \left[\frac{\Phi^m*S_w^n}{a}\right] * \left[\frac{1}{R_w} + \frac{S_{wb}}{S_w}\left[\frac{1}{R_{wb}} - \frac{1}{R_w}\right]\right]$

where:

S_w : Water Saturation of the uninvaded zone.

R_t : True Resistivity of the formation (i.e. deep laterolog or deep induction log).

R_{sh} : Resistivity of shale.

V_{sh} : Volume of shale.

Φ : Porosity.

Φ_e : Effective porosity.

R_w : Formation Water Resistivity at formation temperature.
n : Saturation exponent.
m : Cementation exponent.
a : Tortuosity factor.
B : Normalized equivalent conductance of sodium clay exchange cations.
S_{wb} : Bound water saturation.
R_{wb} : Bound water resistivity.
Q_{vn} : Normalized cation exchange capacity per unit volume.

Some of the aforementioned parameters needed to be determined, and then we can start the calculation of water saturation. These include formation temperature and formation water resistivity.

4.2.5.1 Formation temperature

The importance of formation temperature comes from its influence on the formation water salinity, which controls the resistivity. Thus for valid input values of water resistivity one must correct them to formation temperature, since water resistivity decreases as the temperature increases and vice versa. For all studied wells the following formula was used to determine the formation temperature

$$F_{temp} = TLT + \frac{(BLT - TLT) * (depth - TLI)}{(BLI - TLI)} \tag{4.10}$$

where:
F_{temp} : Formation temperature (degC).
TLT : Top log temperature (degC).
TLI : Top log Interval (m).
BLT : Bottom log temperature (degC).
BLI : Bottom log Interval (m).

4.2.5.2 Formation Water Resistivity

Formation water is defined as the water uncontaminated by the drilling process (invasion of the mud filtrate) that saturates the pores of the formation (Ushie, 2001) . Hence it should be determined accurately for reliable saturation calculation. Several methods could be used to derive formation water resistivity, including the calculation of Spontaneous Potential (SP) log, water catalogue, chemical analysis, water sample measurements, calculation from nearby water bearing formation, from Rwa technique, and from various

cross plots (Opuwari, 2010) . In this project formation water resistivity was derived using Pickett plot due to the lack of the (SP) log.

Pickett plot With the Archie equation considered an essential step from qualitative to quantitative analysis of the well logs. Pickett plot is graphical solution for the Archie equation by plotting formation resistivity against porosity on a double logarithm scale. In other words he rearranges Archie equation as follows:

$$\log \Phi = -\frac{1}{\mathrm{m}} \log \mathrm{R_t} - \mathrm{n} \log \mathrm{S_w} + \log \mathrm{R_w} \tag{4.11}$$

At the fully water saturated intervals the plot should result in straight line with a slope equal to negative (m) through the lowest resistivity values against different values of porosity (Opuwari, 2010). Formation water resistivity value will be the interception at one hundred percent porosity point. At the point where hydrocarbon replaces water the plot will be displaced horizontally to the right due to resistivity increase. Therefore the distance between the point and the one hundred percent water saturation is controlled by water saturation at that point (Krygowski, 2003) . Lines of constant water saturation lie parallel to the one hundred percent water saturation and the separations between those lines depend on the saturation exponent (n).. The values of saturation exponent (n) and cementation exponent (m) are 1.76 and 1.78 respectively as obtained from a special core analysis. The formation water resistivity from the plot is 0.8.

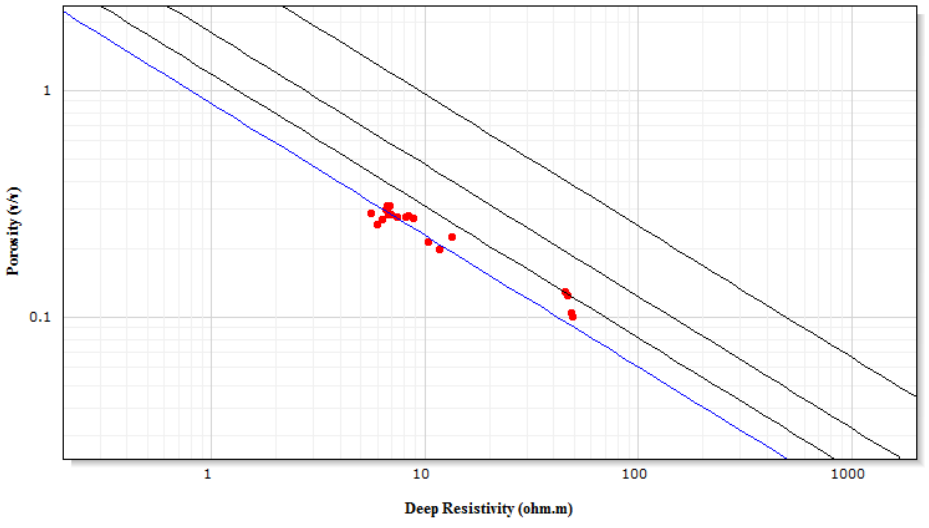

Figure 4.33: Pickett Plot for determination of formation water resistivity

4.2.5.3 Comparison between the saturation models within each Facies, the first approach

Having known that most of the shaly sand saturation models are empirical and fits to local data and lacks universal application, in other words they fit to specific environment. Hence comparison between these models is done within each facies, since these facies reflect different environments. Thus none of the shaly sand saturation models will fit to different environments. The approach is to determine which of these models is most consistent to calculate water saturation within specific facies.

Facies (A) Water saturation outcomes in this facies show that the Archie model is the most consistent model to calculate water saturation. The reason for getting more consistent predictions when using the Archie model and underestimating water saturation predictions when using other shaly sand models could be explained as follows; According to (Lirong et al., 2013) Bentiu and Abu Gabra formation which represent the reservoir units within Muglad Basin composed of high content of K feldspars which is raise the readings of Gamma ray log. This leads to overestimation in the shale content, which is also a lead to higher conductivity. Since Archie model will not account for shale conductivity and consider the water as only conductive fluid in the formation while shaly sand models will account for the shale presence. Hence Archie gives a bit higher readings above the core saturation while water saturation obtained from shaly sand models is below the core saturation.

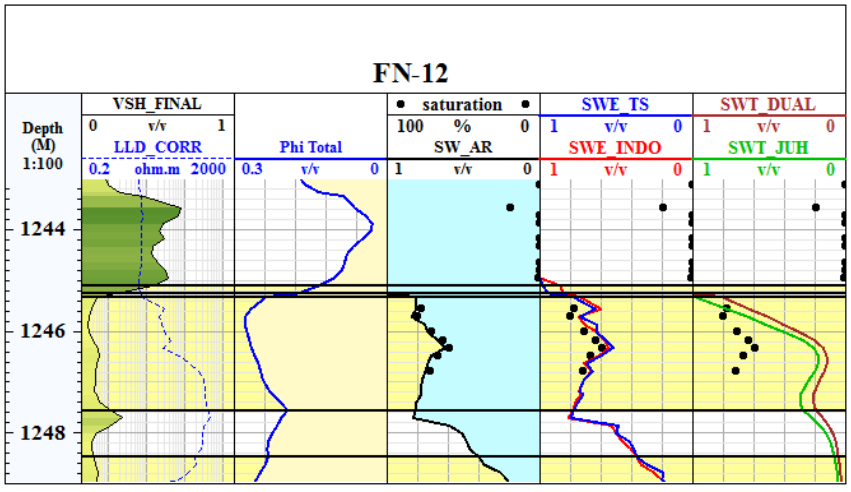

Figure 4.34: Correlation between core water saturation and log saturation within facies (A) cored interval in FN-12

Facies (B) Water saturation outcomes in this facies show that the Simandoux (volume of shale) model is the most consistent model with core data. Water saturation obtained within this facies using Archie and other shaly sand saturation models have given results that are higher than the core saturation data. The reason for getting more consistent predictions when using the Indonesian model and overestimating water saturation predictions when using Archie and other shaly sand models is discussed below It is likely that the Archie equation will overestimate the water saturation as result of considering the shale conductivity as water conductivity. Additionally, the reason for higher water saturation when using the Indonesian model within this facies rather than the Simandoux model is due to the shale term in each conductivity equation of those models. In the Simandoux model conductivity equation has volume of shale Vsh exponent equal to one; while in the Indonesian model conductivity equation has an exponent that is itself a function of volume of shale. This means that the calculated shale conductivity in the Simandoux model is higher than in the Indonesian model. Therefore, the Indonesian model underestimates the water saturation in this case. On the other hand the need of need of CEC measured from rock samples in laboratory environments to calibrate the one that calculated directly from well logs limits the ability of double layer models to give reliable results (Kurniawan, 2005). Having known that shales can be classified into effective shale which has significant (CEC) and passive shale which has essentially zero (CEC) (Hamada 1995). Thus the lack of core calibration of CEC that measured from the continuous log in this project, leading to CEC being measured according to the shale volume not to clay mineralogy. This also explains why the water saturation measured by double layer models increases as the shale increase in each facies.

Facies (C) Water saturation outcomes in this facies show that the Indonesian model is the most consistent model with the core data. As with facies (B) the same argument can be made for the higher water saturation when using the Archie model compared to the core data. The same argument as for facies (B) can be made when comparing the Simandoux and Indonesian saturation outcomes within this facies. It appears that the Simandoux model overestimates the water saturation within this facies due its higher shale conductivity than the Indonesian model. Water saturation obtained using double layer models within this facies is higher than core data, since the CEC is measured according to the shale volume not to clay mineralogy as in facies (B). This also explains why the difference between core saturation and double layer model is higher within this facies than in facies (B).

Facies (D) None of the shaly sand models has given consistent results with core data, this facies has the highest degree of shaliness among the other facies. Hence the

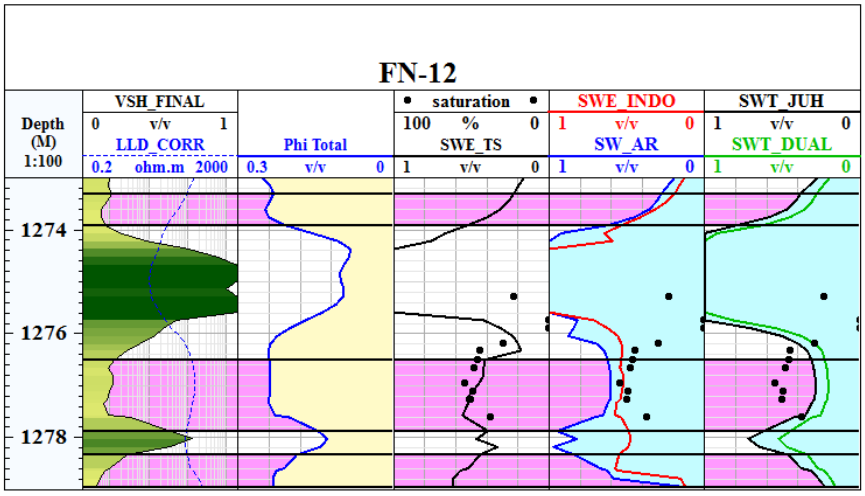

Figure 4.35: Correlation between core water saturation and log saturation within facies (B) cored interval in FN-12

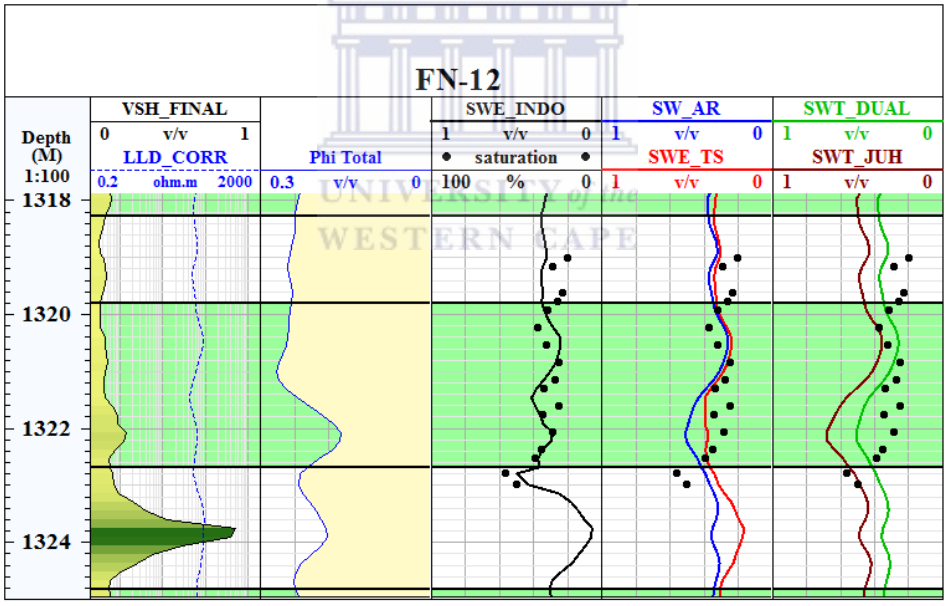

Figure 4.36: Correlation between core water saturation and log saturation within facies (C) cored interval in FN-12

shale models failed to accommodate this facies; since they do not consider the type of shale, only the volume of shale. Therefore they overestimated the water saturation as shale increases within this facies. Further, the limitation of using double layer models mainly due to the need of CEC measured from rock samples has led the models failing to accommodate this facies. This approach has failed to determine reliable water saturation within facies (D). Thus another approach based on artificial neural networks was applied

in the studied reservoir to address the problem of calculating water saturation within facies (D).

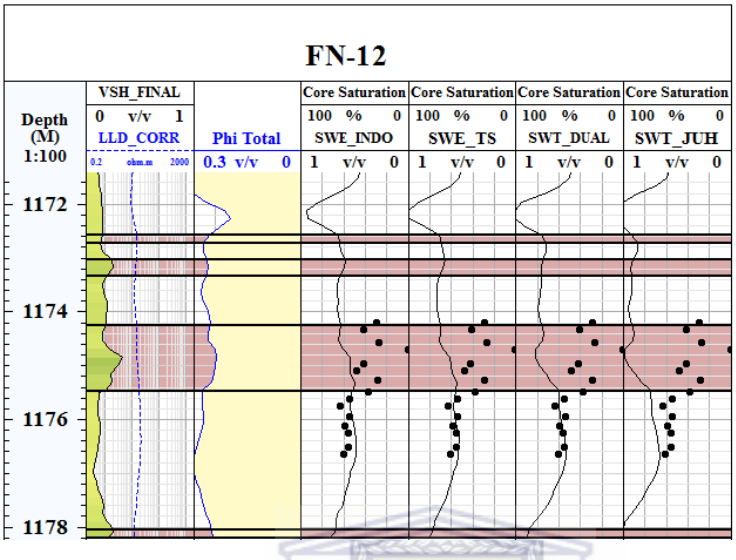

Figure 4.37: Correlation between core water saturation and log saturation within facies (D) cored interval in FN-12

4.2.5.4 Artificial Neural Network model, the second approach

The main objective of using K.mode module in Techlog software is to predict the values of chosen formation property in uncored interval. This would be done by integrating the core data with a combination of well logs. It operates on the principle of back propagation (BP) which is a supervised training technique that sends the input values forward through the network then calculates the difference between the obtained output and corresponding desired output from the training dataset. The error that makes this difference is then propagated backwards through the net, and the weights are adjusted until the calculated output values best approximate the desired values (Zerrouki et al., 2014).

4.2.5.5 The work flow

After checking data quality (editing, depth shifting, and normalization) as discussed in chapter four, the selection of appropriate inputs for the model occurs. This step plays an essential role in model construction. This is due to the strong relation between inputs and outputs reflected in more accurate predictions (Alizadeh et al., 2012; Lim, 2005). Therefore the following logs were used as input parameters to the model according to (Al-Bulushi et al., 2009). These logs represent the primary parameters for water saturation calculation, which are porosity and lithology as well as fluid distribution - Density

- Neutron
- Resistivity
- Photoelectric factor (PEF)

The next step is to adjust model or network structure. The network consists of three components:

- Input layer (the set of chosen well logs for the calculation).
- Hidden layer (the set of particular nodes, each of these nodes combines the input curves into total sum which transfer information from input layer into the model. Then differences between the model and validation data (core data in this case) are used to determine the contribution of each node to the final model (concept of back propagation)).
- Output layer (formation property needed to be obtained).

It is generally recommended that the hidden layer has more nodes than the number of input data. This to allow the model to divide the input data into more parts than input data dimensions to reduce the risk of one node being entirely dominated by a single input curve, in other words to induce weighting them equally in terms of their contribution to the output layer. Therefore the structure 4-8-1 is chosen in this project, which means four inputs, eight hidden nodes, and one property to be calculated. Model structure is shown in Figure (5.33).

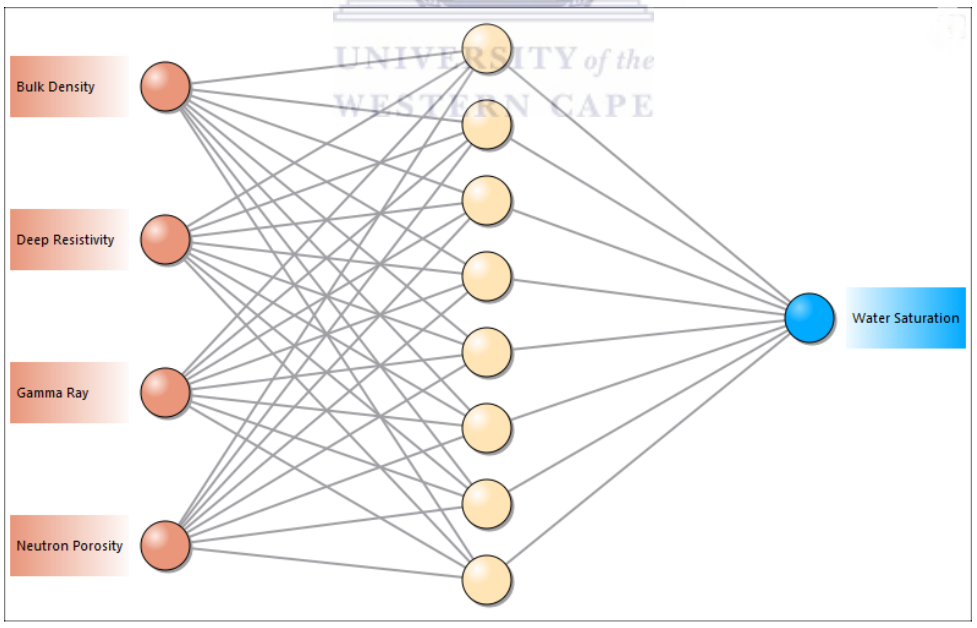

Figure 4.38: chosen model structure 4-8-1

Then the major step is to learn the model. Artificial intelligence is generally divided into two basic categories rule-based (expert) systems and adaptive (neural) systems. In supervised learning, the network is trained with many pairs of input and corresponding

desired output. The outputs of the network are calculated based on provided input by the neurons of the hidden and output layers. Then the calculated outputs will be compared with desired ones to validate the model. The errors are then back-propagated through the network. The model will repeat this process in order to minimize the errors between calculated and desired outputs.

4.2.6 Results

The ANN model successfully predicts water saturation in five core intervals. The correlation between core and ANN model saturation are shown in figures 5.34, 5.35, and 5.36 below.

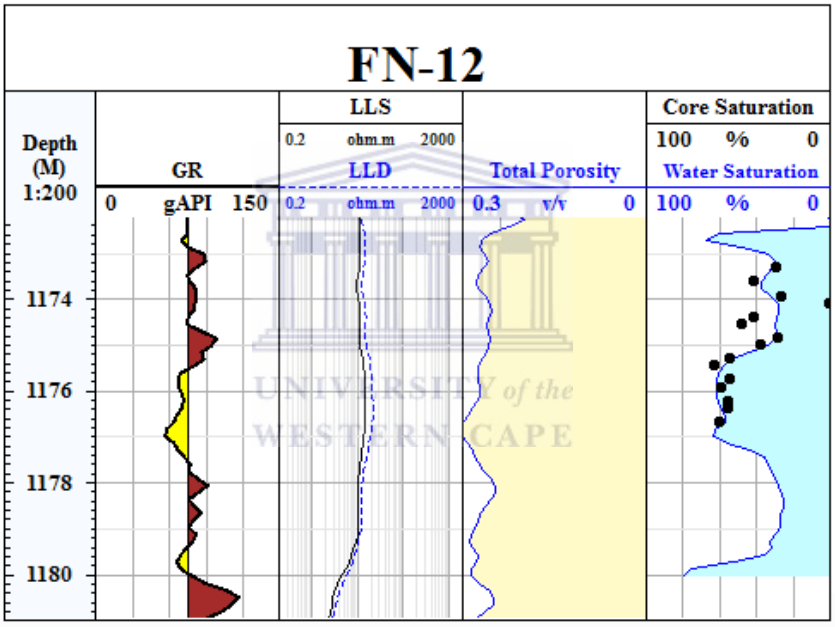

Figure 4.39: Correlation between core and ANN model saturation in core interval one

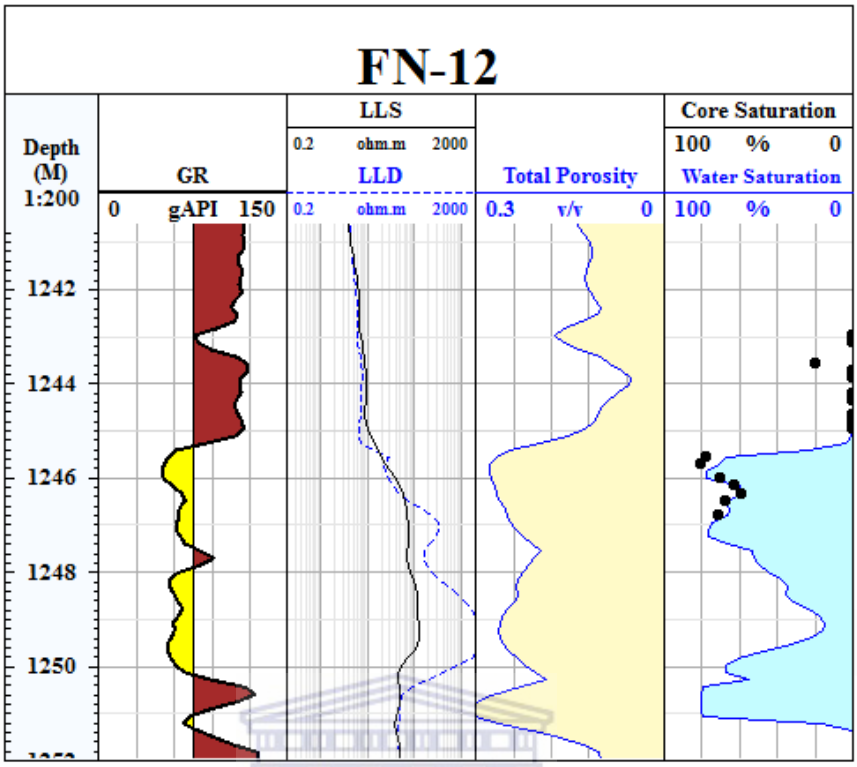

Figure 4.40: Correlation between core and ANN model saturation in core interval two and three

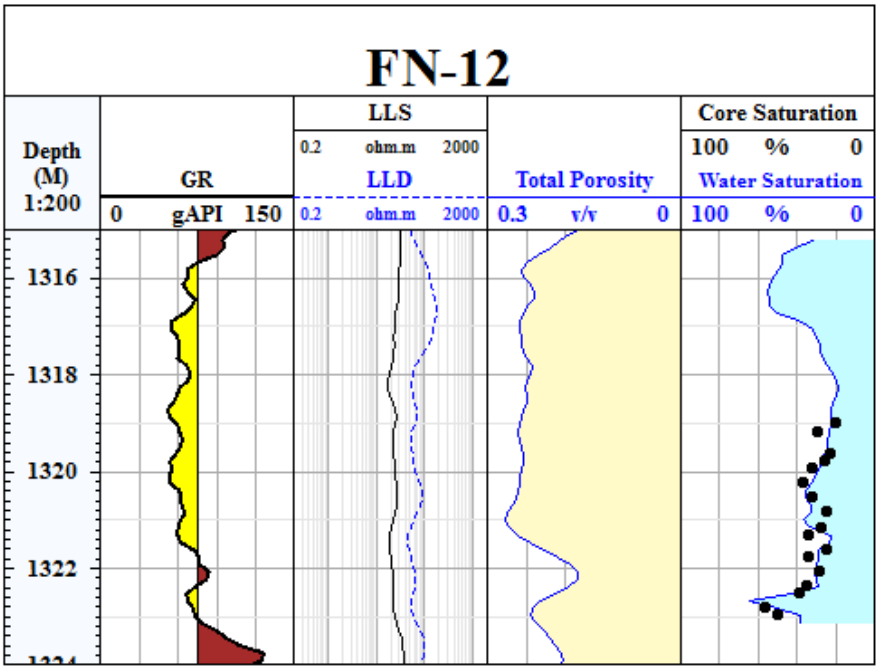

Figure 4.41: Correlation between core and ANN model saturation in core interval five

Chapter 5

Determination of cut-off and net pay

5.1 Net pay and cut-off determination

Estimating hydrocarbon storage or the hydrocarbon in place is an ultimate objective in reservoir characterization. Since the aforementioned estimation will determine the economic viability of the reservoir. To achieve this goal, reservoir interval must be subjected to cutoffs.

5.1.1 Shale volume cut-off

The gross thickness is defined as the interval from the top to the bottom of the reservoir including all non-reservoir rock such as shales. The gross sand refers to the portion of the reservoir which excludes the non-reservoir rock. Hence to eliminate non-reservoir intervals (intervals that have volume of shale more than certain value) the gross sand must be calculated. In other words gross thickness must be subject to some defined or arbitrary shale cutoff. In this study a value of 0.33 was used as shale cut-off.

5.1.2 Permeability and porosity cut-off

The net sand is that fraction of the gross sand that is porous and permeable and contains hydrocarbons and water, and is subject to a defined or arbitrary porosity cut-off. Permeability cut-off is usually the starting point in net pay determinations (Cobb and Marek, 1998) . It is considered as the controlling parameter that directly separate reservoirs from non-reservoir rocks (Widarsono, 2010). Pores with permeability less than cutoff values will not allow fluids to flow. In oil reservoirs permeability cutoff value vary between 1- 10 mD, in this project the permeability cutoff value is considered to be 5 mD as shown in core permeability histogram of FULA - NORTH 12 in figure 6.1.

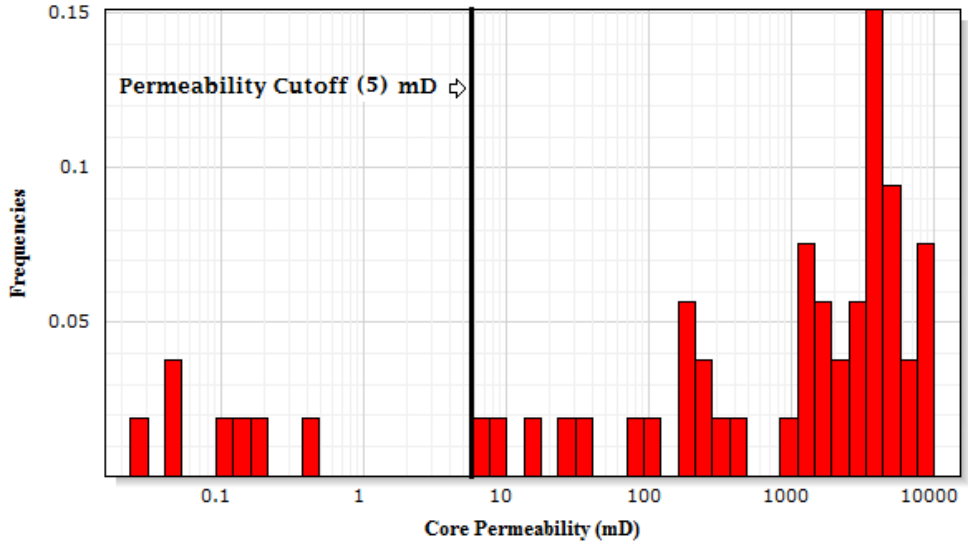

Figure 5.1: Core permeability histogram of the key wells showing the cut-off point.

The determination of porosity cut-off values relies on a generating porosity-permeability relationship from the core measurement. A value of 16% was determined as the porosity cut-off from semi logarithmic porosity vs. permeability cross-plot of the key well as shown in figure 6.2.

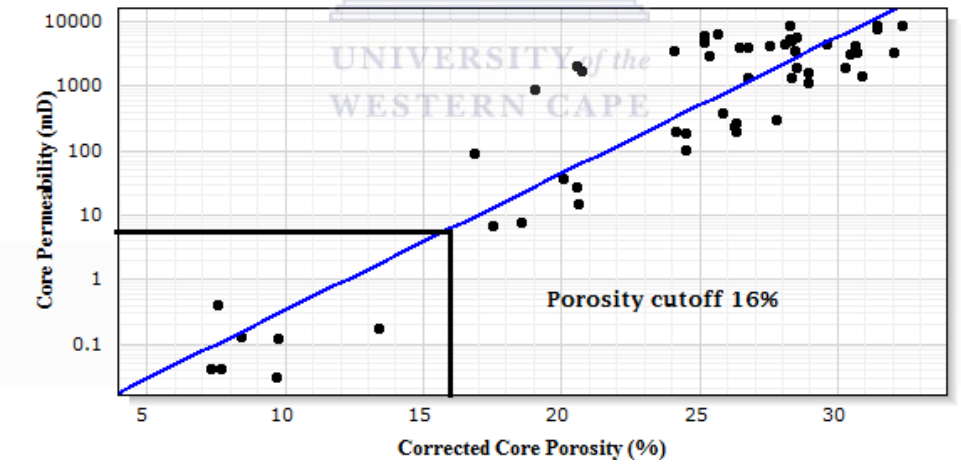

Figure 5.2: Porosity-permeability cross plot to estimate porosity cut-off values

5.1.3 Water saturation cut-off

The net pay is that component of the net sand which contains only hydrocarbons and is subject to water saturation cut-off. A value of 0.65 is used as water saturation cut-off in this study.

5.2 Net pay

In this section, the gross thickness or reservoir intervals were subjected to the predefined cut-off values to obtain the net pay, intervals that contain hydrocarbons with potential economic viability. The calculated cut-off values have been applied to studied reservoirs to determine the net pay within each reservoir. The porosity cut-off (0.16), shale volume cut-off (0.33) and water saturation cut-off (0.65) were used for net pay calculation in this study. The non-net pay intervals were excluded by using a minimum porosity cut-off, maximum shale volume and water saturation cut-off. The obtained results are discussed further in this chapter.

5.2.1 FN-12

As discussed in chapter five, five reservoir zones were identified in the studied interval. For FN-12, the total gross thickness and net pay thickness are 68.33 and 43.804 respectively. The obtained results are given in figures 6.3, 6.4, 6.5, 6.6 and 6.7. Table 6.1 presents the calculated net pay summary for each reservoir with the shale volume, porosity and water saturation.

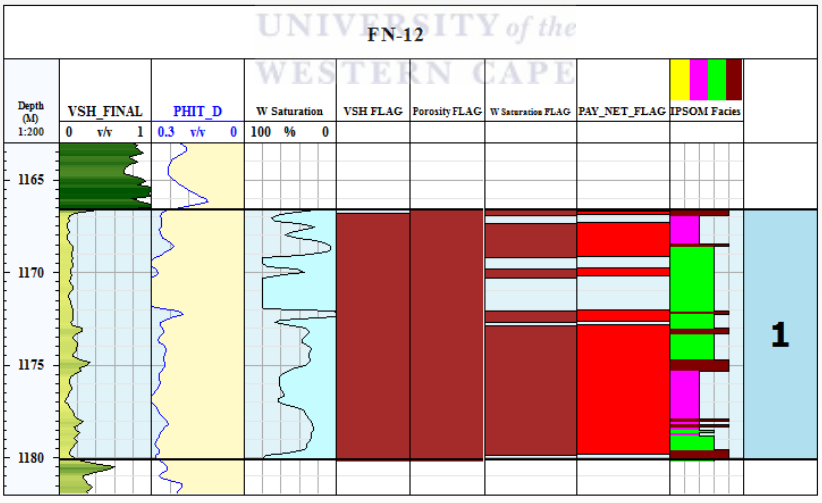

Figure 5.3: Calculated reservoir parameters and net pay interval for reservoir one in FN-12.

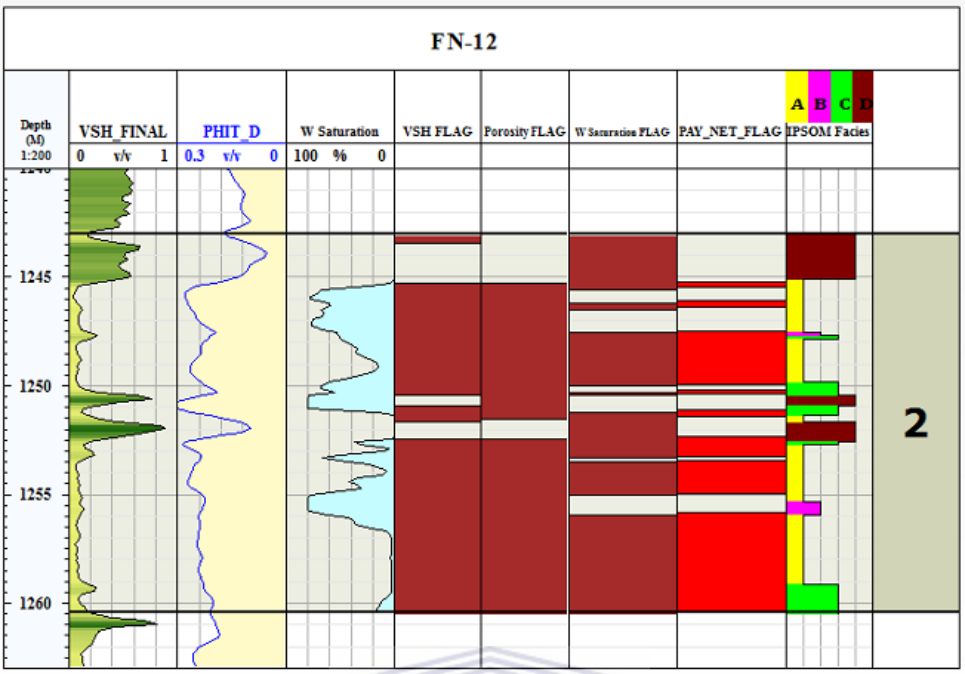

Figure 5.4: Calculated reservoir parameters and net pay interval for reservoir two in FN-12.

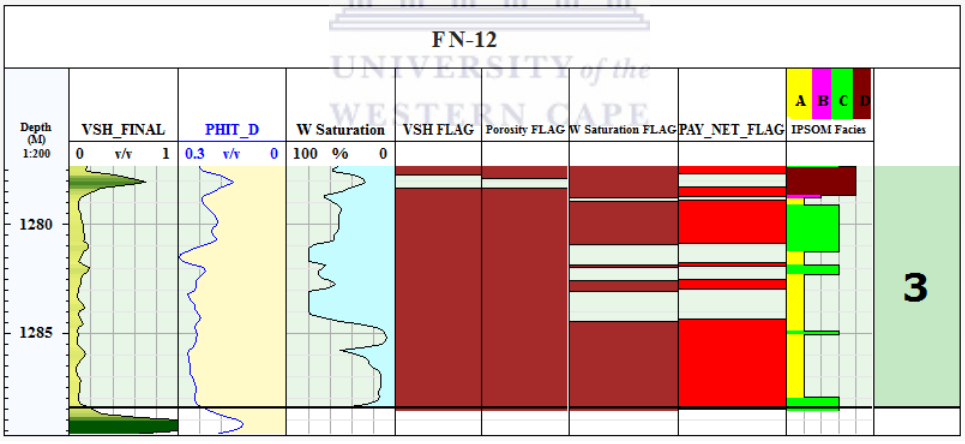

Figure 5.5: Calculated reservoir parameters and net pay interval for reservoir three in FN-12.

Table 5.1: Summary of calculated reservoir pay parameters for FN-12

res	top	bottom	gross	Net	Net-gross	Vsh	porosity	Sw
1	1166.6	1180.06	13.46	10.059	0.747	0.157	0.267	0.379
2	1242.98	1260.38	17.4	10.395	0.597	0.114	0.24	0.227
3	1275.66	1288.4	12.74	8.392	0.659	0.122	0.238	0.367
4	1289.92	1306.7	16.78	7.62	0.454	0.095	0.243	0.263
5	1315.21	1323.16	7.95	7.338	0.923	0.107	0.239	0.34

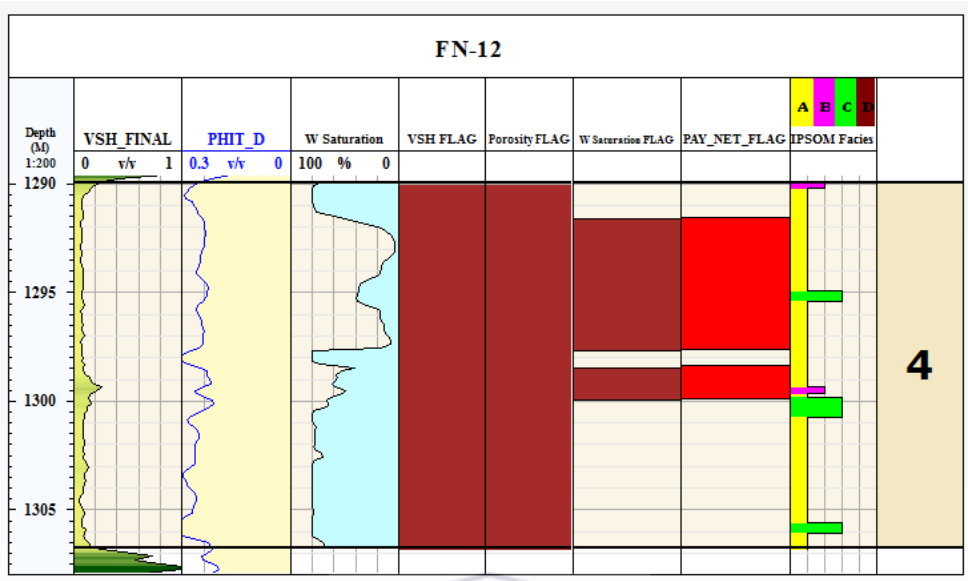

Figure 5.6: Calculated reservoir parameters and net pay interval for reservoir four in FN-12.

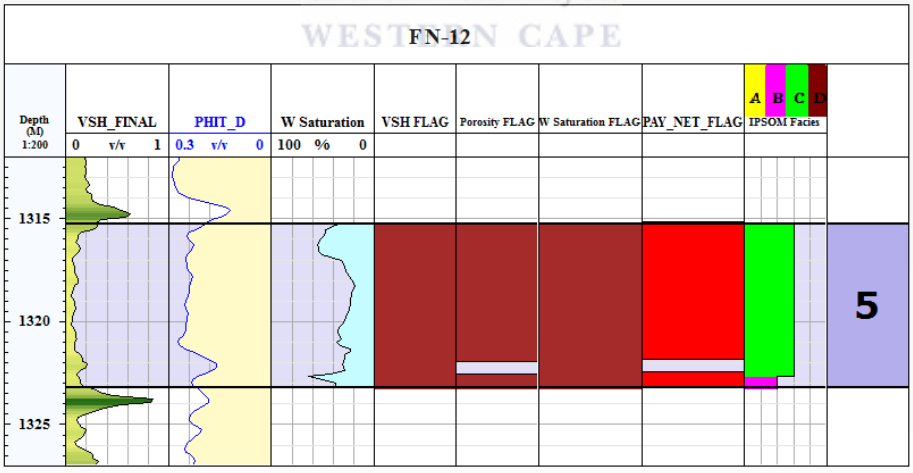

Figure 5.7: Calculated reservoir parameters and net pay interval for reservoir five in FN-12.

5.2.2 FN-92

FN-92 has total gross thickness of 51.13m and a net pay thickness of 42.304m. The obtained results are given in figures 6.8, 6.9, 6.10 6.11 and 6.12. Table 6.2 presents the calculated net pay summary for each reservoir with the shale volume, porosity and water saturation.

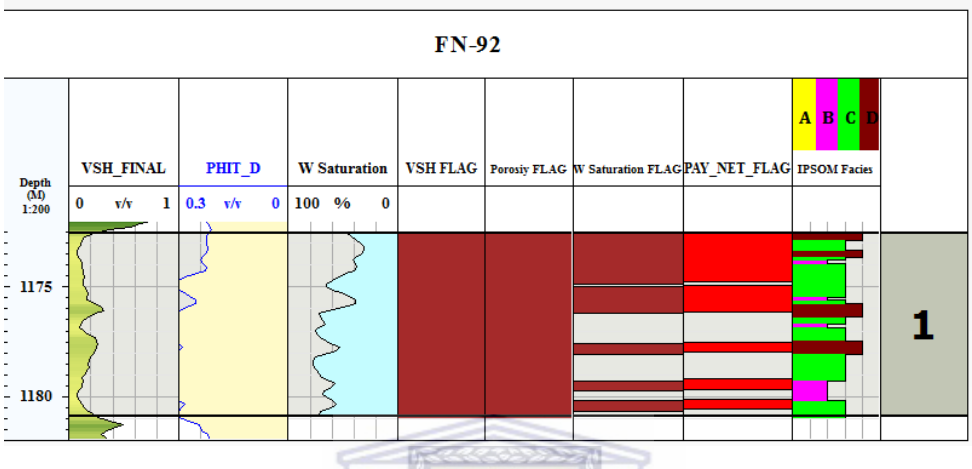

Figure 5.8: Calculated reservoir parameters and net pay interval for reservoir one in FN-92.

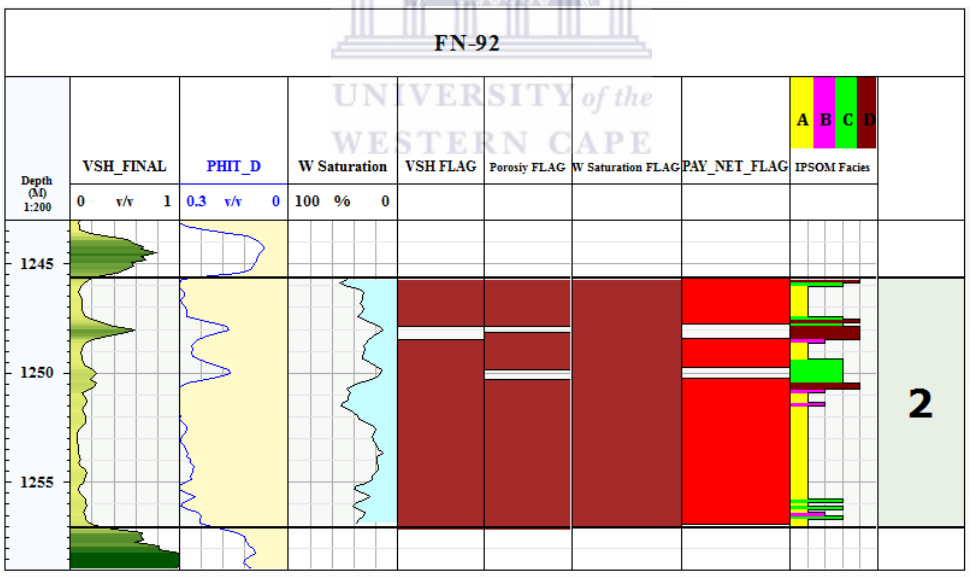

Figure 5.9: Calculated reservoir parameters and net pay interval for reservoir two in FN-92.

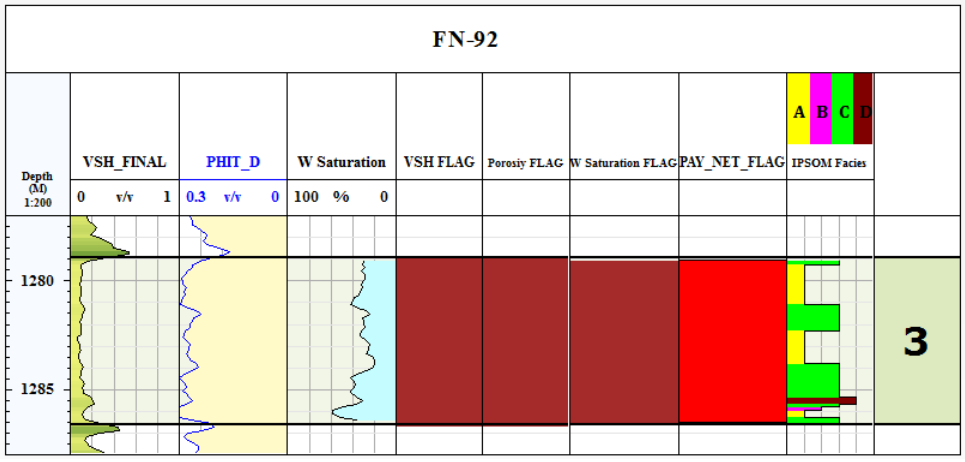

Figure 5.10: Calculated reservoir parameters and net pay interval for reservoir three in FN-92.

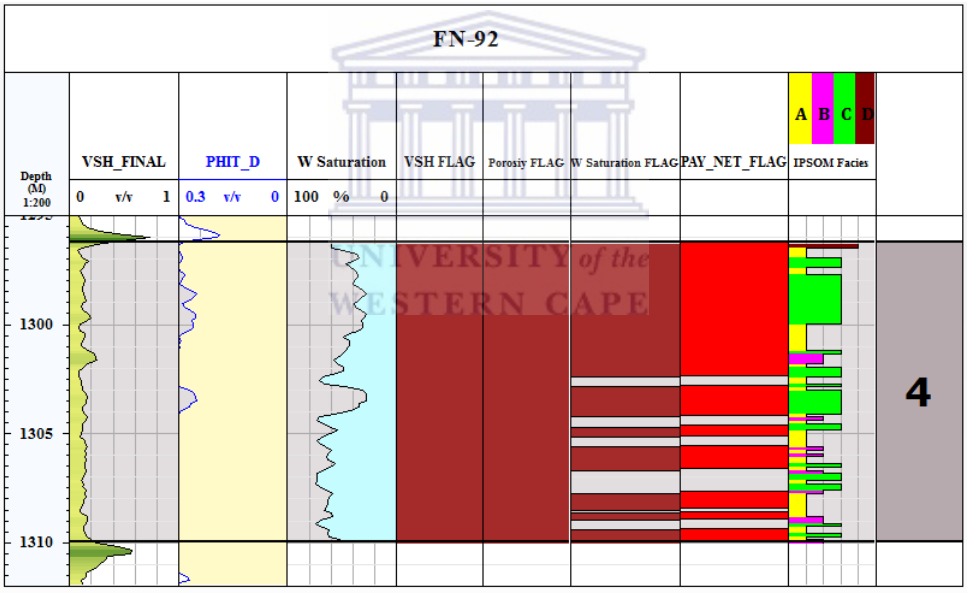

Figure 5.11: Calculated reservoir parameters and net pay interval for reservoir four in FN-92.

Table 5.2: Summary of calculated reservoir pay parameters for FN-92

res	Top	bottom	gross	Net	Net-gross	Vsh	porosity	Sw
1	1172.5	1180.85	8.35	4.877	0.584	0.155	0.269	0.498
2	1245.62	1257.04	11.42	10.211	0.894	0.124	0.281	0.32
3	1278.88	1286.57	7.69	7.468	0.971	0.108	0.279	0.339
4	1296.21	1309.91	13.7	10.548	0.77	0.136	0.331	0.479
5	1314.1	1324.07	9.97	9.2	0.965	0.155	0.245	0.31

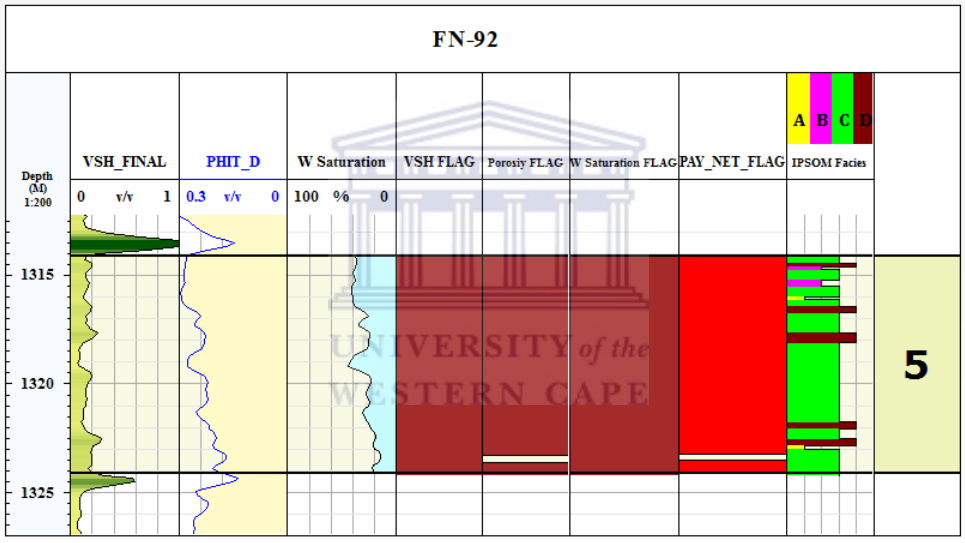

Figure 5.12: Calculated reservoir parameters and net pay interval for reservoir five in FN-92.

5.2.3 FN-10

For FN-10, the total gross thickness and net pay thickness are 78.27 and 73.255 respectively. The obtained results are given in figures 6.13, 6.14, 6.15 6.16 and 6.17. The calculated net pay summary for each reservoir with the shale volume, porosity and water saturation are presented in Table (6.3)

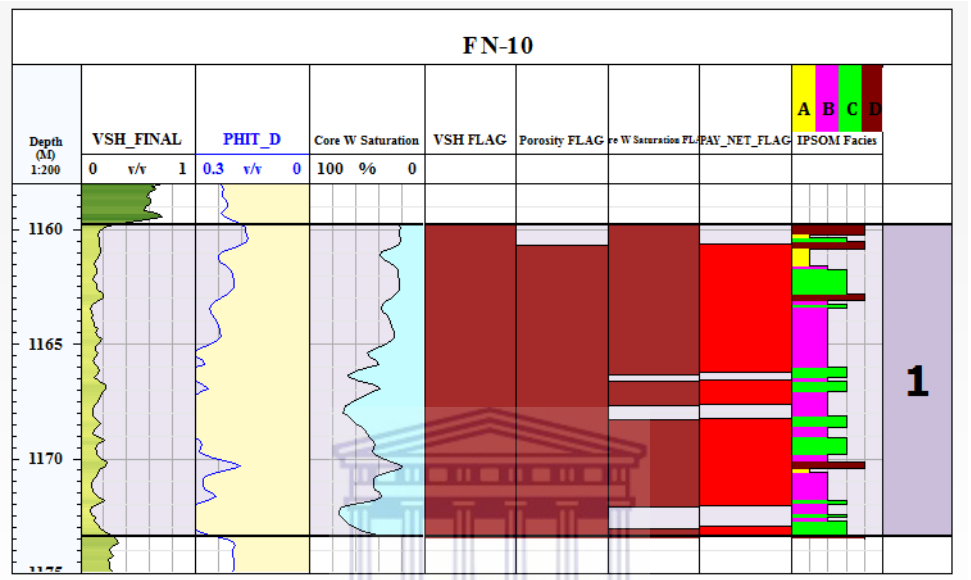

Figure 5.13: Calculated reservoir parameters and net pay interval for reservoir one in FN-10.

Figure 5.14: Calculated reservoir parameters and net pay interval for reservoir two in FN-10.

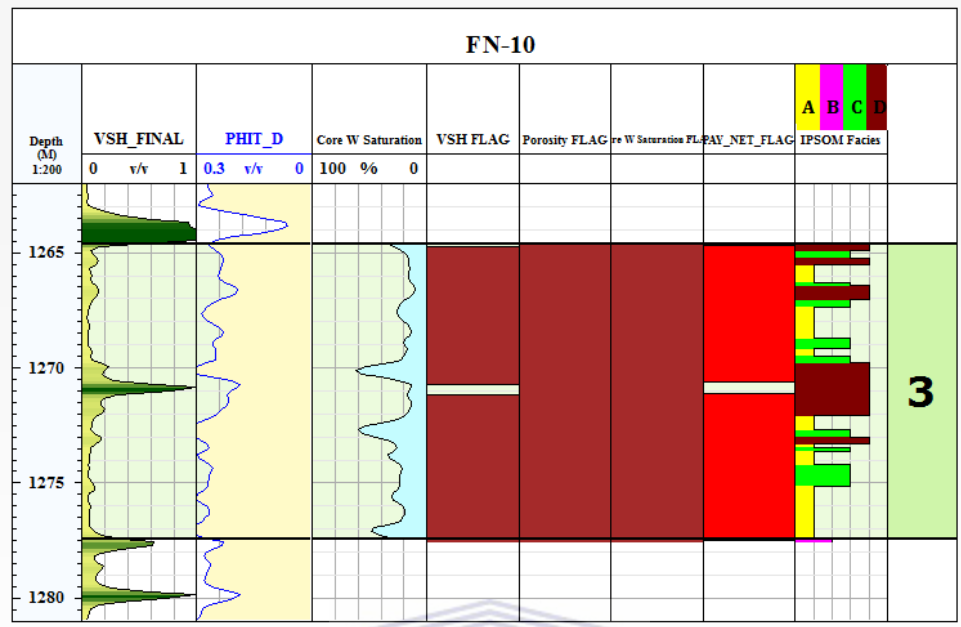

Figure 5.15: Calculated reservoir parameters and net pay interval for reservoir three in FN-10.

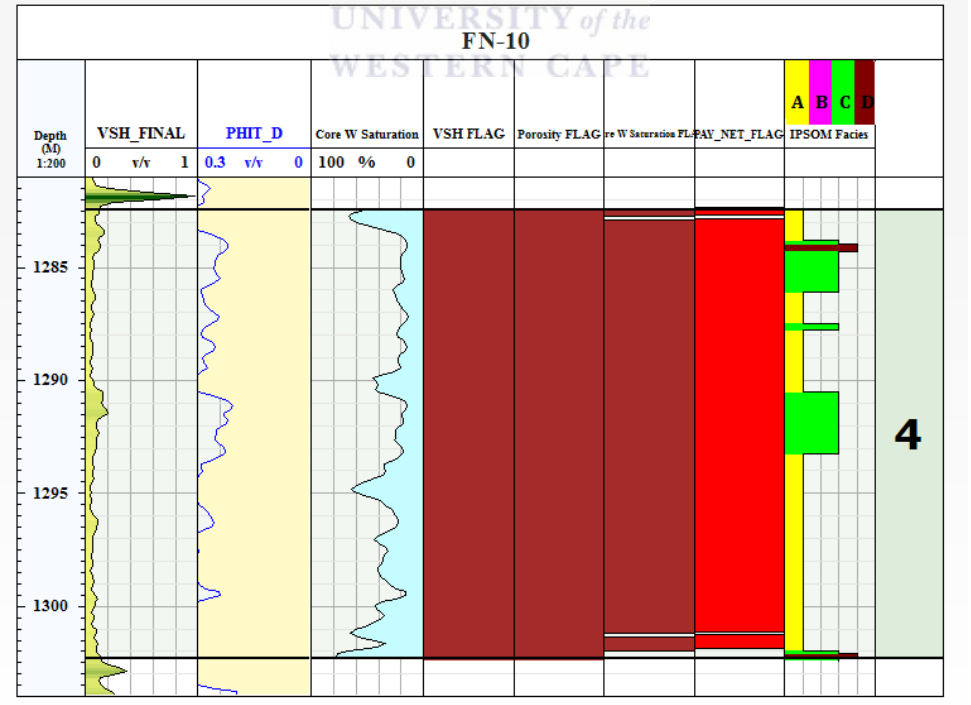

Figure 5.16: Calculated reservoir parameters and net pay interval for reservoir four in FN-10.

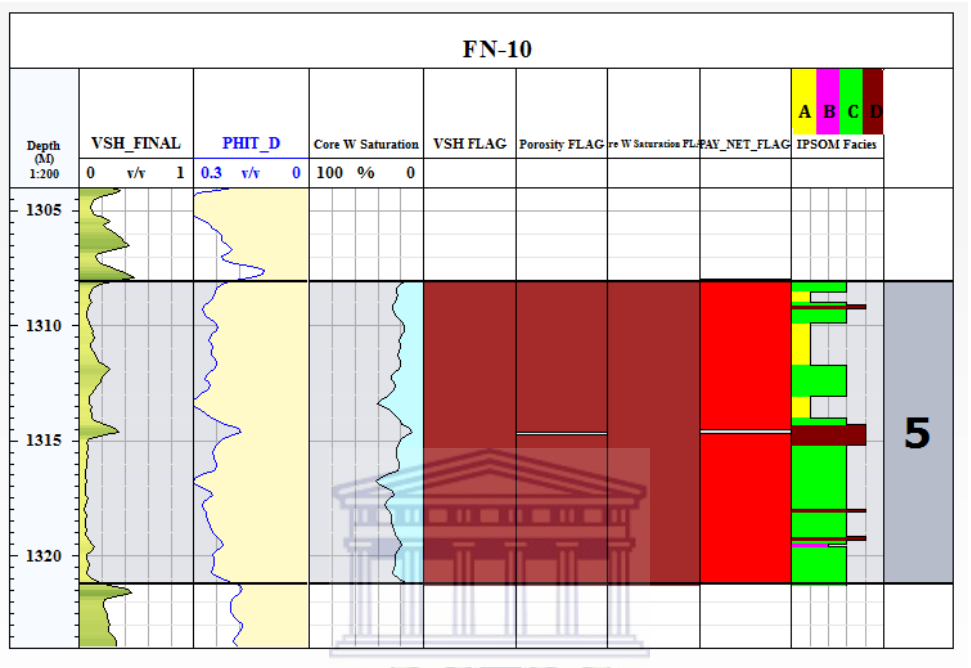

Figure 5.17: Calculated reservoir parameters and net pay interval for reservoir five in FN-10.

Table 5.3: Summary of calculated reservoir pay parameters for FN-10

res	top	bottom	gross	Net	Net-gross	Vsh	porosity	Sw
1	1159.74	1173.37	13.63	10.863	0.797	0.147	0.263	0.411
2	1235.17	1253.97	18.8	18.006	0.958	0.107	0.288	0.314
3	1264.58	1277.43	12.85	12.205	0.95	0.104	0.268	0.272
4	1282.42	1302.27	19.85	19.202	0.967	0.083	0.288	0.323
5	1308.04	1321.18	13.14	12.979	0.988	0.107	0.255	0.254

5.2.4 FN-94

The identified reservoir zones in FN-94 have a total gross thickness and net pay thickness of 61.44m and 54.998m respectively. The obtained results are given in figures 6.18, 6.19, 6.20, 6.21 and 6.22. Table 6.4 presents the calculated net pay summary for each reservoir with the shale volume, porosity and water saturation.

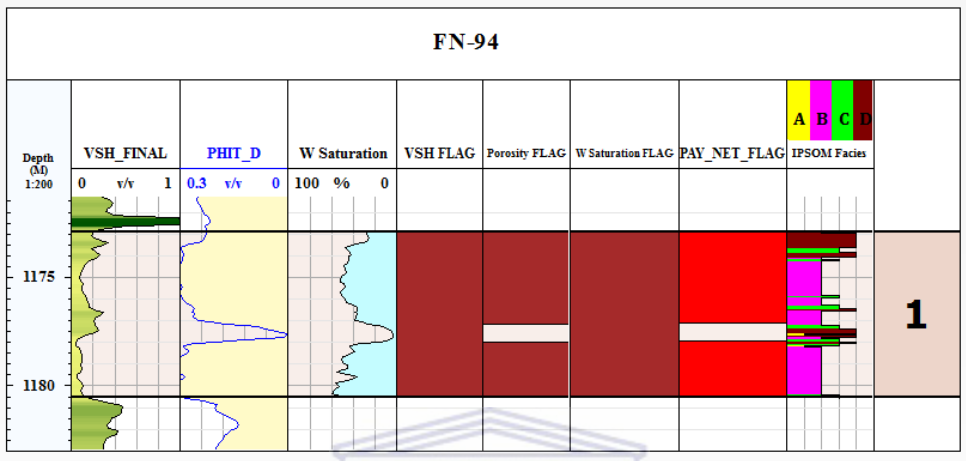

Figure 5.18: Calculated reservoir parameters and net pay interval for reservoir one in FN-94.

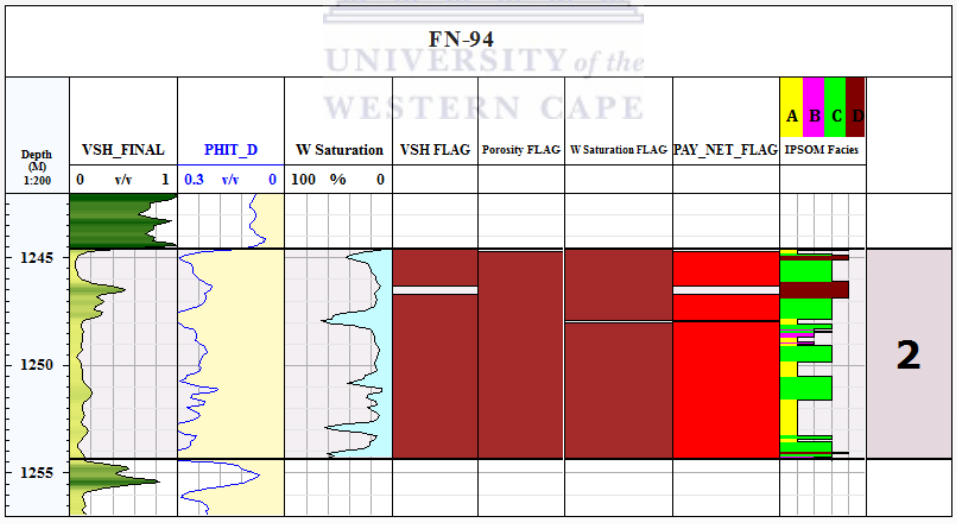

Figure 5.19: Calculated reservoir parameters and net pay interval for reservoir two in FN-94.

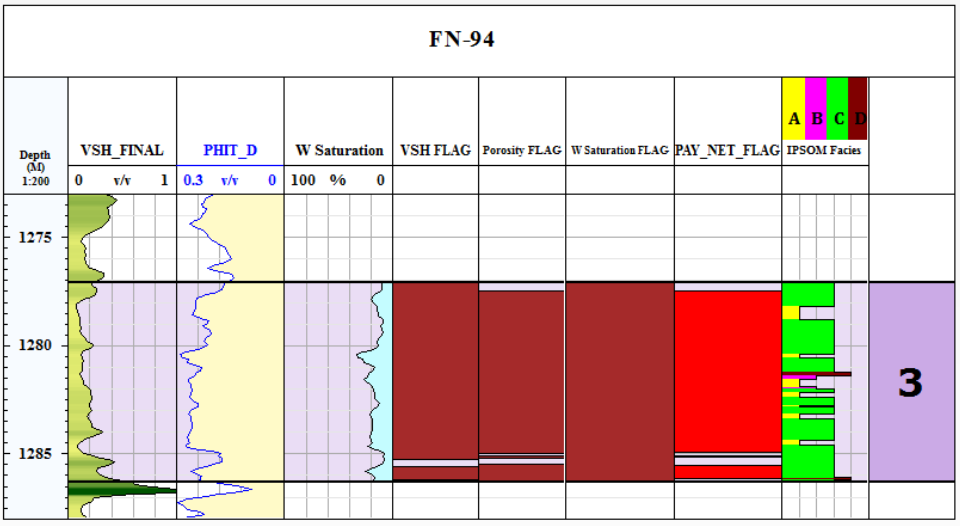

Figure 5.20: Calculated reservoir parameters and net pay interval for reservoir three in FN-94.

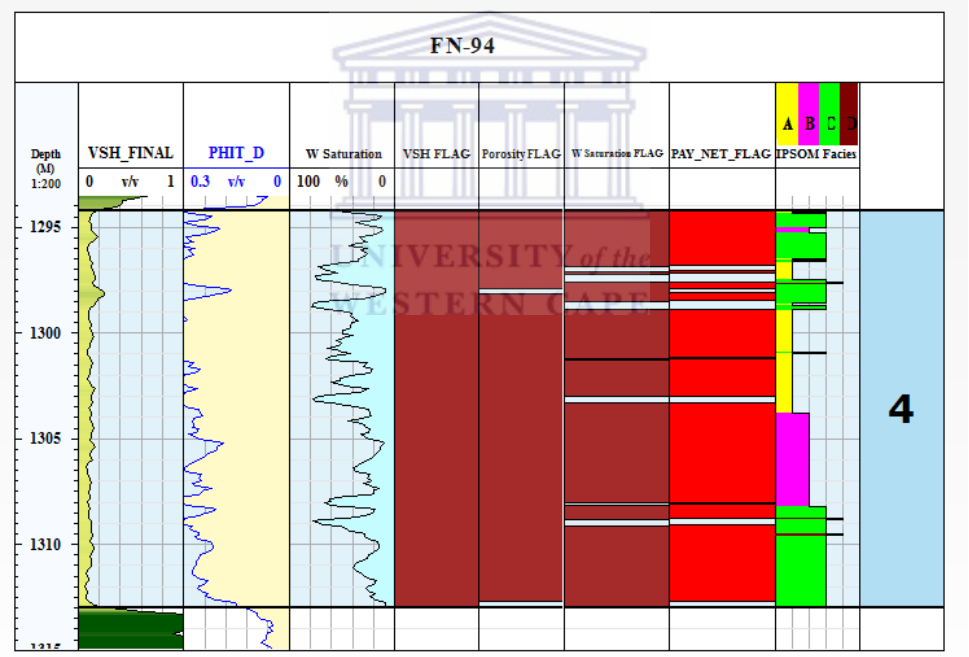

Figure 5.21: Calculated reservoir parameters and net pay interval for reservoir four in FN-94.

Table 5.4: Summary of calculated reservoir pay parameters for FN-94

Reservoir	Top	bottom	gross	net	Net-gross	Vsh	porosity	Sw
1	1172.86	1180.48	7.62	6.771	0.889	0.138	0.29	0.45
2	1244.58	1254.33	9.75	9.146	0.938	0.138	0.26	0.264
3	1277.05	1286.28	9.23	8.153	0.883	0.169	0.246	0.181
4	1294.18	1312.94	18.76	16.535	0.881	0.12	0.275	0.343
5	1322.44	1338.52	16.08	14.393	0.895	0.13	0.251	0.28

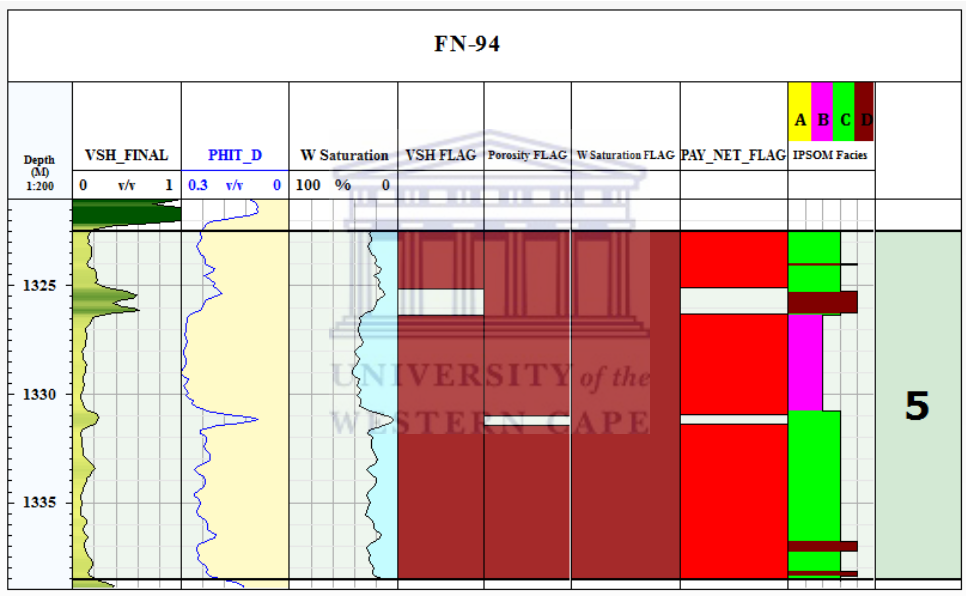

Figure 5.22: Calculated reservoir parameters and net pay interval for reservoir five in FN-94.

Chapter 6

conclusion and recommendations

6.1 conclusion

In this project, comprehensive fluid saturation study for Fula north field in Muglad Basin was carried out using four wells with wireline logs and limited core data.

Four different shaly sand lithofacies (A, B, C, D)were identifed according to lithology discription in the core reports. These lithofacies were used to predict the electrofacies from wireline logs in core surrounding intervals. The classifier used in this prediction resulted in a very good consistency with core facies.

The available data from four wells were comprehensively analyzed to determine the petrophysical parameters.The wireline logs were used to calculate the shale volume, porosity, and water saturation.while the core data was used to validate the obtained parameters.

Another approach that integrate the well logs with core data was used to determine the water saturation in the studied reservoirs to address the complexity of obtaining the water saturation within shaly sand formation. The outcomes of the aforementioned approach was very consistent with core water saturation and used as input parameter for the net pay determination.

Net pay determinations were conducted to distinguish between reservoir and non-reservoir rocks. Cut-off values of 16% for porosity, 33% for shale volume, and 65% water saturation were used. The resulting distribution of these estimated petrophysical parameters suggested that the Fula north fielf in Muglad Basin is a potential field for oil.

6.2 Recommendations

For more reliable petrophysical model, petrophysical parameters must be determined accurately with better quality wireline data and more core measurements.

CEC values must be measured from the rock samples in laboratory environment for accurate estimation of water saturation to confirm the ANN model for water saturation in this study.

Also spectral gamma ray analysis should be carried out for more reliable outcomes for volume of shale.

UNIVERSITY of the
WESTERN CAPE

References

Adeoti, L., Ayolabi, E., and James, P. (2009). An integrated approach to volume of shale analysis: Niger delta example, offrire field. *World Applied Sciences Journal*: *7*(4): 448–452.

Al-Bulushi, N., King, P. R., Blunt, M. J., and Kraaijveld, M. (2009). Development of artificial neural network models for predicting water saturation and fluid distribution. *Journal of Petroleum Science and Engineering*: *68*(3): 197–208.

Al-Saddique, M. A., Hamada, G., and Al-Awad, M. N. (2000). Recent advances in coring and core analysis technology new technique to improve reservoir evaluation. *Engineering journal of the University of Qatar*: *13*.

Ali, J. (1994). Neural networks: a new tool for the petroleum industry? *Society of Petroleum Engineers*.

Alizadeh, B., Najjari, S., and Kadkhodaie-Ilkhchi, A. (2012). Artificial neural network modeling and cluster analysis for organic facies and burial history estimation using well log data: A case study of the south pars gas field, persian gulf, iran. *Computers & Geosciences*: *45*: 261–269.

Amigun, J., Olisa, B., and Fadeyi, O. (2012). Petrophysical analysis of well logs for reservoir evaluation; a case study of laja oil field, niger delta. *Journal of Petroleum and Gas Exploration Research*: *2*(10): 181–187.

Aminian, K. and Ameri, S. (2005). Application of artificial neural networks for reservoir characterization with limited data. *Journal of Petroleum Science and Engineering*: *49*(3): 212–222.

An, L. H. (2000). Neutral network in lithology determination. *Journal of Computer Science and Cybernetics*: *16*(2): 59–62.

Archie, G. E. (1942). The electrical resistivity log as an aid in determining some reservoir characteristics. *Petroleum Technology*: 54–62.

Asquith, G. and Gibson, C. (1982). *Basic well log analysis for geologists*. AAPG.

Bassiouni, Z. (1994). *Theory, Measurement and Interpretation of Well Logs*. 4. The Society of Petroleum Engineers.

Browne, S. and Fairhead, J. (1983). Gravity study of the central african rift system: a model of continental disruption 1. the ngaoundere and abu gabra rifts. *Tectonophysics*: *94*(1): 187–203.

Bush, D. C. and Jenkins, R. E. (1977). Shaly sand log analysis using cation exchange capacity data.

Clavier, Huyle, W., and D., M. (1971). Quantitative interpretation of t.d.t logs; part i and ii. *Journal of Petroleum Technology*: *23*(6): 743–763.

Clavier, C., Coates, G., and Dumanoir, J. (1984). Theoretical and experimental bases for the dual-water model for interpretation of shaly sands. *Society of Petroleum Engineers Journal*: *24*(02): 153–168.

Cobb, W. and Marek, F. (1998). Net pay determination and waterflood depletion mechanisms. *Society of Petroleum Engineers 48952, in the Annual Technical Conference and Exhibition*.

Dubois, M. K., Bohling, G. C., and Chakrabarti, S. (2007). Comparison of four approaches to a rock facies classification problem. *Computers & Geosciences*: *33*(5): 599–617.

Ellis, D. and Singer, J. (2008). *Well Logging for Earth Scientists* (Second edition Netherlands ed.). Springer.

Fairhead, J. (1988). Mesozoic plate tectonic reconstructions of the central south atlantic ocean the role of the west and central african rift system. *Tectonophysics*: *155*(1-4): 181–191.

Gharbi, R. B. and Mansoori, G. A. (2005). An introduction to artificial intelligence applications in petroleum exploration and production. *Journal of Petroleum Science and Engineering*: *49*(3): 93–96.

Giedt, N. R. (1990). Unity field-sudan muglad rift basin, upper nile province. *AAPG Bulletin*: 177–197.

Gifford, C. M. and Agah, A. (2010). Collaborative multi-agent rock facies classification from wireline well log data. *Engineering Applications of Artificial Intelligence*: *23*(7): 1158–1172.

Glover, P. (2013). Petrophysics msc course notes, porosity. University of Leeds.

Gluyas, J. and Swarbick, R. (2004). *Petroleum geoscience*. Oxford: Blackwell Publishing Co.

Gunter, G., Pinch, J., Finneran, J. M., and Bryant, W. T. (1997). Overview of an integrated process model to develop petrophysical based reservoir descriptions. *Society of Petroleum Engineers*: (38748).

Hamada, G. (1996). An integrated approach to determine shale volume and hydrocarbon potential in shaly sand. In *SCA paper 9548, presented at SCA Intl. Symposium*: (pp. 12–14).

Hill, H. J. and Milburn, J. D. (1956). Effect of clay and water salinity on electrochemical behavior of reservoir rocks. *Society of Petroleum Engineers.*: *207*: 65–72.

Hossin, A. (1960). Calcul des saturations en eau par la methode du ciment argileux (formule d'archie generalisee). *Bulletin de L'Association des Technicienes du Petrole*: 140.

Hussien, R. A. (2012). Sequence stratigraphy and sedimentary facies of fula subbasin, muglad basin (sudan). *Journal of Science and Technology*: *13*: 13–25.

Juhasz, I. (1981). Normalised qv;the key to shaly sand evaluation using the waxman-smits equation in the absence of core data. *Society of Petrophysicists and Well Log Analysts. 22nd Annual Logging Symposium*: 1–36.

Kamel., M. H. and Mabrouk., W. M. (2003). Estimation of shale volume using a combination of the three porosity logs. *Journal of Petroleum Science and Engineering*: *40*: 145–157.

Krygowski, D. A. (2003). *Guide to Petrophysical Interpretation*. Austin Texas U.S.A.

Kumar, B. and Kishore, M. (2006). Electrofacies classification - a critical approach. In *Proceedings of the 6th international conference and exposition on petroleum geophysics, Society of Petroleum Geophysicists (SPG), Kolkata, India*: (pp. 822–825).

Kurniawan, F. (2005). *Shaly Sand Interpretation Using CEC-Dependent Petrophysical Parameters*. PhD thesis: Louisiana State University.

Lee, M. W. and Collett, T. S. (2006). A method of shaly sand correction for estimating gas hydrate saturations using downhole electrical resistivity log data. Technical report: U.S. Geological Survey, Scientific Investigations.

Lehmann, K. (2010). Environmental corrections to gamma-ray log data; strategies for geophysical logging with geological and technical drilling. *Journal of Applied Geophysics*: *70*(1): 17–26.

Lim, J.-S. (2005). Reservoir properties determination using fuzzy logic and neural networks from well data in offshore korea. *Journal of Petroleum Science and Engineering*: *49*(3): 182–192.

Lirong, D., Dingsheng, C., Zhi, L., Zhiwei, Z., and Jingchun, W. (2013). Petroleum geology of the fula sub-basin, muglad basin, sudan. *Journal of Petroleum Geology*: *36*(1): 43–59.

Lowell, J. D. and Genik, G. J. (1972). Sea-floor spreading and structural evolution of southern red sea. *AAPG Bulletin*: *56*(2): 247–259.

Makeen, Y. M., Abdullah, W. H., Hakimi, M. H., and Mustapha, K. A. (2015). Source rock characteristics of the lower cretaceous abu gabra formation in the muglad basin, sudan, and its relevance to oil generation studies. *Marine and Petroleum Geology*: *59*: 505–516.

Mohaghegh, S., Arefi, R., Ameri, S., Aminiand, K., and Nutter, R. (1996). Petroleum reservoir characterization with the aid of artificial neural networks. *Journal of Petroleum Science and Engineering*: *16*(4): 263–274.

Mohamed, A. E. and Mohammed, A. S. (2008). Stratigraphy and tectonic evolution of the oil producing horizons of muglad basin, sudan. *Journal of Science and Technology*: *9*(1): 1–8.

Mohamed, A. Y., Ashcroft, W., and Whiteman, A. (2001). Structural development and crustal stretching in the muglad basin, southern sudan. *Journal of African Earth Sciences*: *32*(2): 179–191.

Octavian, C. (2006). *Principles of Sequence Stratigraphy* (First ed.). Elsevier.

Opuwari, M. (2010). *Petrophysical evaluation of the Albian age gas bearing sandstone reservoirs of the OM field, Orange basin, South Africa.* PhD thesis: University of the western cape.

Poupon, A. and Leveaux, J. (1971). Evaluation of water saturation in shaly formations. *Society of Petrophysicists and Well Log Analysts. 12th Annual Logging Symposium.*

Qi, L. and Carr, T. (2006). Neural network prediction of carbonate lithofacies from well logs, big bow and sand arroyo creek fields, southwest kansas. *Computers and Geosciences*: *32*: 947–964.

Quijada, M. F. and Steward, R. (2007). Petrophysical analysis of well logs from manitou lake, saskatchewan. Technical report: CREWERS Research Report.

Rider, M. (1996). *The geological Interpretation of well logs* (Second ed.). Rider-French consulting LTD.

Saggaf, M. M. and Nebrija, L. (2000). Estimation of lithologies and depositional facies from wire-line logs. *AAPG bulletin*: *84*(10): 1633–1646.

Sayed, A. M. I. (2003). *Sedimentology and reservoir geology of the middle-upper cretaceous strata in unity and heglig fields in SE Muglad Rift Basin, Sudan.* PhD thesis: The Faculty of Geotechnical Engineering, Geology and Mining.

Schandelmeier, H., Reynolds, P., and K¨ uster, D. (1993). Spatial and temporal relationship between alkaline magmatism and early rifting in north-central sudan. *Geoscientific Research in Northeast Africa. Balkema*: 221–225.

Schlumberger (1989). *Log Interpretation Charts.* Schlumberger Oilfield Services, Houston.

Schull, T. J. (1988). Rift basins of interior sudan: petroleum exploration and discovery. *AAPG bulletin*: *72*(10): 1128–1142.

Serra, O. (1985). *Sedimentary environments from wireline logs.* Schlumberger Limited.

Shier, D. (2004). Well log normalization: methods and guidelines. *Petrophysics*: *45*(03).

Simandoux, P. (1963). Dielectric measurements on porous media: Application to measurement of water saturation: Study of the behavior of argillacious formation. *Society of Petrophysicists and Well Log Analysts*: 97–124.

Steiber, R. (1973). Optimization of shale volumes in open hole logs. *Journal of Petroleum Technology*: *31*: 147–162.

Tang, H. and White, C. (2008). Multivariate statistical log log-facies classification on a shallow marine reservoir. *Petroleum Science and Engineering*: *61*: 88–93.

Ushie, F. (2001). Formation water resistivity (rw) determination: the sp method. *Applied Environmental Manage*: *3*: 172–177.

Vail, J. (1985). Alkaline ring complexes in sudan. *Journal of African Earth Sciences*: *3*(1): 51–59.

Vail, J. R. (1978). *Outline of the geology and mineral deposits of the Democratic Republic of the Sudan and adjacent areas*. London : HMSO.

Waxman, M. and Smits, L. (1968). Electrical conductivities in oil-bearing shaly sands. *Society of Petroleum Engineers Journal*: *8*: 107–122.

Widarsono, B. (2010). Single or multiple porosity cut-off? a new relevange provided by application of a new approach. *LEMIGAS Scientific Contribution*: *33*(1): 1–8.

Winsauer, W. and McCardell, W. (1953). Ionic double-layer conductivity in reservoir rock. *Journal of Petroleum Technology*: *5*: 129–134.

Worthington, P. F. (1985). The evolution of shaly-sand concepts in reservoir evaluation. *The Log Analyst*: *26*(01).

Yumei, L. (2006). Facies identification from well logs : A comparison of discriminant analysis and naive bayes classifier. *Petroleum Science and Engineering*: *53*: 149–157.

Zerrouki, A. A., Aifa, T., and Baddari, K. (2014). Prediction of natural fracture porosity from well log data by means of fuzzy ranking and an artificial neural network in hassi messaoud oil field, algeria. *Journal of Petroleum Science and Engineering*: *115*: 78–89.

Appendices

Appendix A

Well FN-12 Core Gamma Ray Results

Well FN-12 Raw core measure ments

UNIVERSITY of the
WESTERN CAPE

Table 1: Well FN-12 Core Gamma Ray Results

Depth	GR	Depth	GR	Depth	GR	Depth	GR
meter	API	meter	API	meter	API	meter	API
1173.73	10.6	1242.41	179.1	1274.5	194.7	1318.75	37.4
1173.75	10.6	1242.5	179.1	1274.55	196.3	1318.79	43.1
1173.87	46.5	1242.54	126.3	1274.65	196.3	1318.93	43.5
1174	46.5	1242.67	126.3	1274.79	181.4	1319	43.5
1174.01	72.1	1242.75	125.6638	1274.9	181.4	1319.08	37.4
1174.15	64.9	1242.8	125.155	1274.94	183.4463	1319.23	36.9
1174.25	64.9	1242.93	124.9	1275.08	185.0312	1319.25	36.9
1174.29	87.1	1243	124.9	1275.1	186.3	1319.37	40
1174.43	113.6	1243.06	93.2	1275.23	174.2	1319.5	40
1174.5	113.6	1243.19	93.2	1275.25	174.2	1319.52	48
1174.57	54.8	1243.25	93.2	1275.37	174.2	1319.67	38.9
1174.71	79.5	1243.32	126.5	1275.5	156.765	1319.75	38.9
1174.75	79.5	1243.58	159.6	1275.52	137.1637	1319.82	42.8
1174.85	87.1	1243.72	159.6	1275.66	117.5097	1319.96	61.6
1174.99	88.6	1244.24	137.6	1275.81	113.6	1320	66.2
1175	88.6	1244.31	138.0918	1275.82	113.6	1320.11	66.2
1175.13	103.4	1244.39	139.073	1275.95	72.1	1320.25	43.9
1175.25	132.7	1244.5	140.0541	1276.02	72.71883	1320.26	43.9
1175.27	132.7	1244.54	140.3	1276.1	73.9837	1320.4	64.2
1175.41	87.7	1244.69	140.3	1276.24	75.24516	1320.5	110.6
1175.5	38.3	1244.84	149	1276.25	76	1320.55	110.6
1175.55	38.3	1244.9	145.9	1276.39	76	1320.7	86.1
1175.69	43.7	1244.99	131.8	1276.5	126.9	1320.75	86.1
1175.75	46.96667	1245	98.6	1276.53	126.9	1320.84	72.5
1175.83	51.86666	1245.14	24.00901	1276.68	97.8	1320.99	66.8
1175.97	39.4	1245.29	26.1	1276.75	97.8	1321	66.8
1176	40.76667	1245.3	25.4	1276.8	97.8	1321.14	43.1
1176.11	35.3	1245.44	32.23333	1317.61	40.3	1321.25	43.1
1176.25	27.86667	1245.5	47.96667	1317.75	40.3	1321.29	58.2
1176.26	15.8	1245.59	67.39999	1317.76	51.7	1321.44	14.8
1241.5	7.7	1245.74	62.13333	1317.9	41.9	1320.7	86.1
1241.56	7.7	1245.75	51.46667	1318.05	44.7	1320.75	86.1
1241.63	69.3	1245.87	31.7	1318.09	44.7	1320.84	72.5
1241.75	69.3	1273.92	48.5	1318.2	43.3	1320.99	66.8
1241.76	69.3	1273.95	48.5	1318.25	43.3	1321	66.8
1241.89	164.1	1274.07	183.9	1318.35	42.7	1321.14	43.1
1242.02	164.1	1274.21	183.9	1318.49	41.9	1321.25	43.1
1242.12	164.1546	1274.35	186.6784	1318.5	41.9	1321.29	58.2
1242.15	164.1909	1274.36	190.6892	1318.64	37.4	1321.44	14.8

Table 2: Raw core measurements

depth	Grain density	permaebility	porosity	water saturation	oil saturation
meter	gm/cm3	MD	%	%	%
1172.75	2.62	148	31.0	28.9	62.9
1173.00	2.63	130	30.9	40.9	52.9
1173.25	2.63	116	31.0	26.6	66.9
1173.50	2.61	NPP	17.2	0.0	87.2
1173.75	2.65	575	31.5	41.5	53.0
1174.00	2.59	84.4	30.4	47.6	49.7
1174.25	2.64	40.3	28.8	28.4	64.1
1174.50	2.61	238	32.7	37.4	53.6
1174.75	2.66	1069	36.4	54.4	39.0
1175.00	2.62	628	36.2	63.0	31.7
1175.25	2.64	1242	33.5	53.9	43.8
1175.50	2.62	858	33.6	58.7	38.4
1175.75	2.65	303	34.1	55.5	39.5
1176.00	2.64	1340	34.1	54.9	40.3
1176.25	2.63	1405	33.4	60.3	36.0
1241.56	2.68	0.01	8.7	0.0	86.4
1241.75	2.61	NPP	9.6	0.0	94.0
1242.12	2.70	2.14	20.5	19.4	57.6
1242.32	2.59	<0.01	11.2	0.1	96.2
1242.50	2.58	0.30	10.5	0.2	85.8
1242.75	2.66	0.02	9.0	0.0	82.4
1243.00	2.68	0.02	9.9	0.0	92.5
1243.25	2.69	0.02	8.3	0.0	94.8
1243.50	2.63	<0.01	11.1	0.0	89.0
1243.72	2.62	0.03	8.5	0.4	89.2
1244.31	2.63	3158	38.2	77.4	16.5
1244.50	2.63	NPP	37.1	80.0	15.9
1244.90	2.63	6799	33.3	70.5	22.4
1245.00	2.64	1951	24.1	63.1	32.3
1245.30	2.65	5175	29.6	59.0	35.2
1245.50	2.64	4560	37.1	66.9	27.1
1245.75	2.63	3099	31.8	71.3	22.5
1273.95	2.63	3.17	21.7	22.6	67.2
1274.35	2.65	0.06	8.6	0.0	93.5
1274.55	2.65	0.04	12.0	0.0	79.5
1274.90	2.61	6.97	24.1	29.3	58.1
1275.10	2.62	1368	35.7	44.6	49.4
1275.25	2.64	44.8	28.8	45.6	49.0
1275.50	2.61	5.76	24.2	47.7	47.3
1275.82	2.62	NPP	20.2	54.3	40.5
1276.02	2.70	0.14	15.5	49.0	46.1
1276.25	2.63	89.4	28.4	49.9	45.5
1276.50	2.63	1170	35.9	52.6	43.8
1276.75	2.62	11.9	23.5	37.2	55.8

depth	Grain density	permaebility	porosity	water saturation	oil saturation
1317.61	2.63	3327	33.3	20.0	71.9
1317.75	2.62	2952	32.4	28.7	66.8
1318.09	2.64	2774	34.9	22.9	70.9
1318.25	2.63	3175	37.8	25.6	68.1
1318.50	2.63	1559	31.5	31.4	62.4
1318.75	2.63	652	30.2	36.9	57.4
1319.00	2.63	652	31.1	32.0	61.9
1319.25	2.63	1187	29.6	24.5	70.7
1319.50	2.62	3356	36.1	27.0	68.8
1319.75	2.63	4745	33.6	33.3	60.2
1320.00	2.64	2572	33.1	24.5	69.4
1320.25	2.64	3308	33.4	34.0	61.4
1320.50	2.66	37.7	19.7	28.4	65.4
1320.75	2.65	801	24.3	34.7	59.6
1321.00	2.62	462	29.8	38.8	57.0
1321.25	2.64	2247	28.3	56.0	36.1
1321.44	2.65	NPP	22.3	49.6	44.1

UNIVERSITY of the
WESTERN CAPE